Correlation between sea-level rise and aspects of future tropical cyclone activity in CMIP6 models

Joseph Lockwood[1], Michael Oppenheimer[2], Ning Lin[1], Robert E Kopp[3], Gabriel Vecchi[1], and Avantika Gori[1]

[1]Princeton University
[2]Princeton U
[3]Rutgers University

November 22, 2022

Abstract

Future coastal flood hazard at many locations will be impacted by both tropical cyclone (TC) change and relative sea-level rise (SLR). Despite sea level and TC activity being influenced by common thermodynamic and dynamic climate variables, their future changes are generally considered independently. Here, we investigate correlations between SLR and TC change derived from simulations of 26 Coupled Model Intercomparison Project Phase 6 (CMIP6) models. We first explore correlations between SLR and TC activity by inference from two large-scale factors known to modulate TC activity: potential intensity (PI) and vertical wind shear. Under the high emissions SSP5-8.5, SLR is strongly correlated with PI change (positively) and vertical wind shear change (negatively) over much of the western North Atlantic and North West Pacific. To explore the impact of the joint changes on flood hazard, we then conduct climatologyhydrodynamic modeling with New York City (NYC) as an example. Coastal flood hazard at NYC correlates strongly with global mean surface air temperature (GSAT), due to joint increases in both sea level and TC storm surges, the later driven by stronger and more slowly moving TCs. If positive correlations between SLR and TC changes are ignored in estimating flood hazard, the average projected change to the historical 100 year storm tide event is under-estimated by 0.09 m (7%) and the range across CMIP6 models is underestimated by 0.17 m (11 %). Our results suggest that flood hazard assessments that neglect the joint influence of these factors and that do not reflect the full distribution of GSAT changes will not accurately represent future flood hazard.

Correlation between sea-level rise and aspects of future tropical cyclone activity in CMIP6 models

Joseph W. Lockwood[1], Michael Oppenheimer[1,2,3], Ning Lin[4], Robert E. Kopp[5,6], Gabriel A. Vecchi[1,3,7] and Avantika Gori[4]

[1]Department of Geoscience, Princeton University, NJ 08544, USA
[2]Princeton School of Public and International Affairs, Princeton University, Princeton, NJ 08544, USA
[3]High Meadows Environmental Institute, Princeton, NJ, USA
[4]Civil and Environmental Engineering, Princeton University, Princeton, NJ 08544, USA
[5]Institute of Earth, Ocean, and Atmospheric Sciences, Rutgers University, 71 Dudley Road, Suite 205, New Brunswick, NJ 08901, USA
[6]Department of Earth and Planetary Sciences, Rutgers University, Piscataway, NJ, USA
[7]Atmospheric and Oceanic Sciences Program, Princeton University, Princeton, NJ, USA

Key Points:

- Relative sea-level rise at many locations is strongly correlated with two large-scale factors known to modulate tropical cyclone activity
- Joint increases in sea level and tropical cyclone activity with global mean temperature substantially compound flood hazard at New York City
- Flood hazard assessments that neglect the joint influence of these factors may not accurately represent future flood hazard

Corresponding author: Joseph W. Lockwood, `jl115@princeton.edu`

Abstract

Future coastal flood hazard at many locations will be impacted by both tropical cyclone (TC) change and relative sea-level rise (SLR). Despite sea level and TC activity being influenced by common thermodynamic and dynamic climate variables, their future changes are generally considered independently. Here, we investigate correlations between SLR and TC change derived from simulations of 26 Coupled Model Intercomparison Project Phase 6 (CMIP6) models. We first explore correlations between SLR and TC activity by inference from two large-scale factors known to modulate TC activity: potential intensity (PI) and vertical wind shear. Under the high emissions SSP5-8.5, SLR is strongly correlated with PI change (positively) and vertical wind shear change (negatively) over much of the western North Atlantic and North West Pacific. To explore the impact of the joint changes on flood hazard, we then conduct climatology–hydrodynamic modeling with New York City (NYC) as an example. Coastal flood hazard at NYC correlates strongly with global mean surface air temperature (GSAT), due to joint increases in both sea level and TC storm surges, the later driven by stronger and more slowly moving TCs. If positive correlations between SLR and TC changes are ignored in estimating flood hazard, the average projected change to the historical 100 year storm tide event is underestimated by 0.09 m (7 %) and the range across CMIP6 models is underestimated by 0.17 m (11 %). Our results suggest that flood hazard assessments that neglect the joint influence of these factors and that do not reflect the full distribution of GSAT changes will not accurately represent future flood hazard.

Plain Language Summary

Future coastal flood hazard at many locations will be influenced by sea level rise (SLR) and tropical cyclone (TC) activity. Due to their common dependence on the wider climate system, TC activity and SLR may increase in a joint manner with progressive warming, potentially acting to compound local flood hazards. To explore joint variability, we first analyze correlations between SLR and future TC activity by inference from two large-scale climate factors known to modulate TC activity. Our results indicate that flood hazard in the western North Atlantic and North West Pacific will increase with progressive warming, due to concurrent changes in relative SLR and TC activity. Using a set of realistic synthetic TC events and a storm tide model, we find that joint increases in SLR and TC activity substantially compound flood hazard at New York City, with TC surge changes driven by progressively slower and stronger TCs. Our results suggest that flood hazard assessments that neglect the joint influence of these factors and that do not reflect the full distribution of global mean surface temperature (that modulates joint changes in TC and SLR) will not accurately capture future flood hazard.

1 Introduction

Coastal flooding in the context of future tropical cyclone (TC) variability, sea-level rise (SLR) and shoreline change is one of the most important issues facing coastal populations (Woodruff et al., 2013). Climate change is increasing the threat posed by TCs to coastal regions (Reed et al., 2015; Wang & Toumi, 2021; Camargo & Wing, 2021; Knutson et al., 2020), with future flood events driven by TC storm surges expected to intensify into the future as a result of accelerated SLR (Lin et al., 2012; Woodruff et al., 2013; Bilskie et al., 2014, 2016; Reed et al., 2015; Garner et al., 2017; Vousdoukas et al., 2018; Marsooli et al., 2019; Idier et al., 2019; Liu et al., 2019; Kirezci et al., 2020; Marsooli & Lin, 2020; De Dominicis et al., 2020). At many locations, future flood hazard may also be compounded by changes in TC climatology and associated storm surges (Lin et al., 2012; Reed et al., 2015; Little et al., 2015; Lin et al., 2016; Buchanan et al., 2016; Marsooli et al., 2019; Marsooli & Lin, 2020), with SLR elevating the baseline on which these events occur. The potential compound effect of sea level change and TC activity is best exemplified by supertyphoon Haiyan (2013). Observed increases in regional sea surface temperatures (SST) and ocean heat content since 1993, likely contributed to both the typhoon's extreme wind speeds and regional SLR. This regional SLR meant that Haiyan's extreme storm surge was on a baseline sea level some 30 cm above levels in 1993 (Trenberth et al., 2015).

Most recent flood hazard assessments generally assume that SLR and TCs are independent, conditional on the emissions pathway (Lin et al., 2012; Garner et al., 2017; Idier et al., 2019; Marsooli et al., 2019; Marsooli & Lin, 2020). Assessments that explore projected changes in TCs generally either combine storm surges with a limited number of SLR scenarios (Lin et al., 2012; Bilskie et al., 2014, 2016; Idier et al., 2019; Liu et al., 2019) or with probabilistic SLR projections that are derived in part from a subset of AOGCMs (Lin et al., 2016; Garner et al., 2017; Vousdoukas et al., 2018; Marsooli et al., 2019; Marsooli & Lin, 2020). On the other hand, assessments that evaluate changes in flood hazard due to SLR usually assume that the statistical nature of TC storm surges will remain unchanged (Hunter, 2011; Tebaldi et al., 2012; Buchanan et al., 2016; Rasmussen et al., 2018; Kopp et al., 2014, 2017; Frederikse et al., 2020; Kirezci et al., 2020). By neglecting concurrent changes (Hunter, 2011; Tebaldi et al., 2012; Buchanan et al., 2016; Rasmussen et al., 2018; Kopp et al., 2014, 2017; Frederikse et al., 2020; Kirezci et al., 2020) or by assuming independence conditional on the emissions scenario (Lin et al., 2012; Garner et al., 2017; Idier et al., 2019; Marsooli et al., 2019; Marsooli & Lin, 2020), assessments may fail to fully represent compounding of future flood hazard.

Recent research shows that dependence structures between climate variables often strongly affects the occurrence frequency and intensity of multivariate extremes (Little et al., 2015; Wahl et al., 2015; Zscheischler & Seneviratne, 2017; Zscheischler et al., 2018). At present, there is limited analysis of the dependence between SLR and TC activity, and its implications for coastal flood hazard. Little et al. (2015) project changes in surge hazard focusing on sterodynamic SLR, composed of ocean thermal expansion and regional ocean steric and dynamic effects (Gregory et al., 2019), and power dissipation index (PDI) changes at 5 sites along the US East Coast — the latter derived from a 15-member ensemble of climate models following a statistical modeling approach (Villarini & Vecchi, 2013). Sterodynamic SLR and PDI projections along the US East Coast are found to be correlated, with joint increases compounding projected flood hazard. However, the projected increases in Atlantic PDI have considerable uncertainty, as several other TC modeling studies using dynamical, rather than statistical, downscaling approaches project little change or decreases in PDI (Yamada et al., 2010; Knutson et al., 2015) .

Joint variability between SLR and TCs will be driven in part by atmospheric warming, which will increase SLR through ocean heat uptake and thermal expansion and by melting land ice (Church et al., 2013; Oppenheimer et al., 2019) as well as the theoretical maximum wind speed (the potential intensity; PI) of TCs in some regions (Vecchi & Soden, 2007a, 2007c; Emanuel, 2013; Sobel et al., 2016). Basin-specific changes in vertical wind shear, another important large-scale variable modulating TC activity, are projected with warming, with increases across the tropical North Atlantic and decreases across the northern tropical Pacific and western North Atlantic (Vecchi & Soden, 2007a, 2007c; Camargo, 2013; Vecchi et al., 2019), which would suggest less conducive conditions for TC activity in the former and more conducive conditions in the latter.

Considerable uncertainty remains in the projection of future TCs, particularly regarding changes in frequency, translation speed and average latitude at which TCs reach their lifetime-maximum intensity (Knutson et al., 2020), and their dependence on the large-scale climate. Low-resolution AOGCMs, which are often used to investigate TCs, generally cannot resolve category 3–5 TCs or poorly simulate the frequency and spatial distribution of category 3–5 TCs compared to observations (Vecchi et al., 2019; Knutson et al., 2020; Yin et al., 2020). These low resolution AOGCMs generally project decreases in global TC frequency under climate change (Knutson et al., 2020). In contrast, some studies project no change (Camargo, 2013; Vecchi et al., 2019) or increases in global TC frequency (Emanuel, 2013; Bhatia et al., 2018; Vecchi et al., 2019; Emanuel, 2021). As reviewed by Knutson et al. (2020), there is moderately strong consensus on a model-projected increase in high intensity TCs, in TCs rainfall and in an increase in storm-surge flooding due to SLR, assuming all other factors are unchanged.

Superimposed on the global SLR, that is driven by ocean thermal expansion and by melting land ice loss, relative sea levels may change owing to vertical land movement (VLM) and dynamic sea level changes. The sterodynamic component of relative SLR is derived from AOGCMs that do not simulate SLR contributions from melting land ice and local non-climatic SLR associated with VLM and glacial isostatic adjustment (GIA) (Kopp et al., 2014, 2015; Griffies et al., 2016; Gregory et al., 2019). Estimates of land ice contributions to SLR are instead derived from physical models of varying degree of complexity (Levermann et al., 2020; Oppenheimer et al., 2019) or from results of structured expert elicitation (Bamber et al., 2019). In probabilistic analyses, variance in global mean sea level rise (GMSLR) and local SLR at many locations in the early 21st century relates predominately to sterodynamic SLR, due to large AOGCM spread in projected changes (Kopp et al., 2014, 2017). In the global average and at many locations, the Antarctic ice-sheet is the dominant source of variance in late 21st century SLR projections (Kopp et al., 2014, 2017).

Although there is strong confidence in accelerated SLR intensifying TC storm surge into the future, only a limited number of studies have assessed the role of their joint changes to future multivariate extreme events, in part due to the large uncertainties discussed above. The questions to be answered in this paper are as follows: (i) Are relative SLR and aspects of TC activity (PI and vertical wind shear) correlated within the wider climate system, and what are the time scales and emissions scenarios over which these correlations apply? (ii) Do the broad-scale joint changes translate into meaningful differences in flood hazards at a local scale? To answer these questions, we first investigate correlations between relative SLR and TC activity derived from simulations of 26 CMIP6 models, across a range of emissions scenarios. We next conduct climatology–hydrodynamic modeling for eight CMIP6 models under SSP5-8.5 to quantify the impact of joint changes to future coastal flood events, as an example, for New York City (NYC).

2 Methods

CMIP6 models comprise a range of AOGCMs and Earth System Models (ESMs), differing from each other in terms of model structure, including vertical coordinate, grid resolution and sub-grid parameterizations (Eyring et al., 2016). We limit our analysis to models that have the variables necessary to compute PI, relative SLR and vertical wind shear. We use only a single run ('r1i1p1') for each CMIP6 model. Change is calculated as the difference between years 1994-2014 of the historical simulation and years 2080-2100 of the high emissions SSP5-8.5, unless otherwise stated. Our primary focus on SSP5-8.5, which has unrealistically high anthropogenic carbon dioxide emissions (Hausfather & Peters, 2020), allows us to maximize the signal of interest. To explore the time periods and scenarios over which these correlations apply, we also calculate relative SLR and PI over years 2014-2100 of the SSP1-2.6, SSP2-4.5 and SSP5-8.5 scenarios for 11 CMIP6 models. These 11 models span the full range of GSAT changes projected by the 26 CMIP6 models used in this study (Fig. S1 a). The goal of our SLR projections is to produce SLR projections consistent with the GSAT of each model. We note that the methods used to project SLR have considerable uncertainties; however, we choose to choose to focus on the mean projection for each model.

2.1 SLR projections

2.1.1 Sterodynamic sea-level change

Sterodynamic SLR (ΔZ(r)) is calculated as the linear addition of changes in ocean dynamic sea level ($\Delta\ \zeta$) and global thermosteric sea level (Δh_θ) following Gregory et al. (2019). It can be diagnosed from CMIP6 model variables as the sum of the changes in zos ($\Delta\ \zeta$(r)) and zostoga ($\Delta\ h_\theta$):

$$\Delta Z(r) = \Delta\zeta(r) + \Delta h_\theta \tag{1}$$

Dynamic sea level fluctuations, due to regional ocean steric and dynamic effects, are calculated as the local height of the sea surface above the geoid with zero global mean (Gregory et al., 2019), so that it measures sea-level pattern fluctuations around the ocean geoid defined via a resting ocean state at z = 0, as defined in Griffies and Greatbatch (2012) and Griffies et al. (2014). As some models used in this study do not have zostoga output, we calculate h_θ using potential temperature (Text S1.1).

2.1.2 Antarctic Ice Sheet

To derive future Antarctic Ice Sheet (AIS) dynamical SLR estimates we utilize the impulse response functions by Levermann et al. (2020). Specifically, Levermann et al. (2020) related subsurface ocean warming in Antarctica to projected GSAT change based on an ensemble of CMIP5 models. Estimated basal melt sensitivities from observations were then used to translate subsurface ocean warming into basal ice-shelf loss projections using 16 ice-sheet models that form part of the Linear Antarctic Response Model Intercomparison Project (LARMIP-2).

Following Levermann et al. (2020), we estimate AIS contributions using an ice shelf melt rate of 8 m year^{-1} for each CMIP6 model (Fig. S2). We note that these estimates have considerable uncertainties related to basal ice shelf melt rates, ice sheet models and scaling factors (Fig. S2). We convert global barystatic contributions to regional values using the output from a Gravitation, Rotation, and Deformation (GRD) model (Tamisiea & Mitrovica, 2011), assuming uniform mass loss for each individual region. The regional imprint of mass loss from the Amundsen sector and the Antarctic peninsula are based on uniform mass loss from West Antarctica. The contribution from East Antarctica and the Weddell and Ross sector is distributed based on the assumption of uniform mass loss from East Antarctica.

In assuming linear response theory, this method is able to capture complex temporal responses of the ice sheets, but neglects any self-dampening or self-amplifying processes. Neglecting self-amplifying processes is particularly relevant in situations in which an instability is dominating the ice loss such as during Marine Ice Sheet Instability (MISI) and Marine Ice Cliff Instability (MICI), although there remains major uncertainty in the possibility of rapid and/or irreversible ice losses via these mechanisms (Fox-Kemper et al., 2021).

The observed evolution of the Amundsen Sea Embayment (ASE) glaciers is compatible with, but not unequivocally indicating an ongoing MISI (Rignot et al., 2014; Joughin et al., 2014; Fox-Kemper et al., 2021). There remains significant discrepancies in projections of MISI due to poor understanding of mechanisms and lack of observational data to constrain ice-sheet models, and it is not expected that widespread loss from the large ice shelves buttressing the bulk of West Antarctic Ice Sheet' will occur before the end of the 21st century (Fox-Kemper et al., 2021). The International Panel on Climate Change (IPCC) Sixth Assessment Report (AR6) (Fox-Kemper et al., 2021) assigned limited agreement (with an assessed likelihood of 0-33%) between studies regarding the exact MICI mechanism and limited evidence (likelihood of 0-33%) of its occurrence in the present or the past, meaning that MICI considered to be characterized by deep uncertainty, and its potential to affect future sea level rise is currently highly uncertain (Oppenheimer et al., 2019; Edwards et al., 2021; Fox-Kemper et al., 2021). These strong caveats that are associated with the approach utilized here, that neglects MISI and MICI, may lead to an underestimation of future dynamical ice loss. Nonetheless, this method provides model specific estimates of Antarctica's future dynamical contribution to SLR.

Following the International Panel on Climate Change (IPCC) Sixth Assessment Report (AR6) (Fox-Kemper et al., 2021), we augment LARMIP-2 estimates with surface mass balance (SMB) estimates. SMB estimates derived directly from GCMs often involve several compromises related to their coarse resolution and their low sophistication to represent important physical processes of polar regions. In addition, SMB consists of multiple components, all of which depend on complex interactions between the atmosphere and the snow/ice surface, large-scale atmospheric circulation and ocean conditions, and ice sheet topography (Kittel et al., 2021). As a result of the complex nature of SMB estimation, and the fact that many GCMs tend to overestimate annual precipitation values over ice-sheets, likely due to poor representation of coastal topography (Genthon et al., 2009), this study parameterizes SMB to estimate SLR contributions for the AIS. Parameterizations are derived from relationships between SMB changes and atmospheric temperature using high resolution regional climate models. For each model, we average estimates derived from the parameterizations of Gregory and Huybrechts (2006) and Kittel et al. (2021) to estimate AIS SMB changes (Text S1.2).

2.1.3 Greenland Ice Sheet

Simulating the changes in continental-scale mass balance (MB) in Greenland Ice Sheet (GIS) models remains challenging due to the small scale of key physics, such as fjord circulation and plume dynamics, and poor understanding of critical processes, such as calving and submarine melting. Fürst et al. (2015) used ten different CMIP5 AOGCMs simulations to provide MB and ocean forcing for their GIS model, accounting for influences of warming subsurface ocean temperatures and basal lubrication on ice dynamics. We model GIS loss using estimates from Fürst et al. (2015), where GIS MB can be estimated as a cubic function of near-surface temperature anomaly over the GIS (Fig. S3):

$$\Delta MB_{GIS} = 0.030T^2_{GrIS} - 0.81T_{GrIS} + 2.2 \tag{2}$$

where TAS_{GrIS} is the average anomaly in near-surface temperature over the GIS.

In Greenland, faster-than-projected changes in mass loss might occur into the future (Aschwanden et al., 2019; Khan et al., 2020) due to cloud processes in polar areas (Hofer et al., 2019) and feedbacks between surface melt and the increasing albedo from meltwater, detritus and pigmented algae (Cook et al., 2020). Warming-induced dynamical changes in atmospheric circulation could enhance summer blocking and produce more frequent extreme melt events over Greenland that may also enhance future mass loss (Delhasse et al., 2018).

2.1.4 Glaciers and Ice Caps

Over the past century, glaciers and ice caps (GIC) have added more mass to the ocean than the GIS and AIS combined. However, the total remiaing mass of glaciers is small by comparison, equivalent to only 0.32 m mean SLR if only the fraction of ice above sea level is considered (Farinotti et al., 2019). We model GIC following Perrette et al. (2013), where the rate of glacier's ice loss is proportional to a change in GSAT:

$$\frac{dV}{dt} = b_o(T - T_o)(1 - \frac{V_{gl}}{V_o})^n \tag{3}$$

where b_o is the global SMB sensitivity, V_{gl} and V_o are the projected and present global glacier volumes (in sea level equivalent) respectively, and n is the scaling coefficient between global glacier area and volume, approximately equal to 1.65 (Perrette et al., 2013). T is the GSAT change as compared to the 1994-2014 historical temperature (T_o). The spatial pattern used here assumes a fixed distribution of the ratios of glacier mass loss between the glacier regions based on the projected distribution in 2100 under Representative Concentration Pathway 8.5 (RCP8.5) (Church et al., 2013). Previous analysis showed that this pattern does not vary much over the 21st century and the mass loss is closely related to the initial glacier mass for a given region. Recent studies have shown that the mass loss distribution to be model and scenario dependent (Hock et al., 2019; Marzeion et al., 2020).

2.1.5 Non-climatic SLR

Changes in land water storage, through groundwater depletion and reservoir impoundment, may have influenced twentieth-century sea-level change but are expected to be relatively minor contributors (Church et al., 2013). We adopt the methods of Kopp et al. (2014) to model land water storage change. Ongoing GIA also leaves its imprint in the spatial pattern of sea-level change, associated with the adjustment of Earth's lithosphere and viscous mantle material to past changes in ice loading since the last glaciation (e.g., Tamisiea and Mitrovica (2011)). This adjustment process gives rise to areas of upward and downward VLM, and the associated mass redistribution also influences Earth's rotation and gravity field with additional impacts on local mean sea level. We use global GIA estimates based on the ICE-6G_C model of Peltier et al. (2015), which uses a wide range of observational constraints, including data from Global Positioning System receivers and time-dependent gravity observations from both surface measurements and the satellite-based Gravity Recovery and Climate Experiment (Argus et al., 2014; Peltier et al., 2015). This data set was sourced from `https://www.atmosp.physics.utoronto.ca/~peltier/data.php`. We note that this term is not relevant to our analysis, since it is independent of climate forcing and constant across models, but does affect projections of flood risk in NYC.

2.2 Large-scale factors affecting TC activity

As low-resolution climate models are better able to simulate the large-scale environment, rather than individual TCs, many studies have chosen to analyze large-scale variables known to be associated with TC activity, instead of modeling TCs directly (Camargo, 2013; Tang & Camargo, 2014; Vecchi et al., 2019; Emanuel, 2021). Following Bister and Emanuel (1998), we calculate PI as a function of both the SST and the vertical profiles of temperature and humidity in the atmosphere. Although PI is a prediction only of the maximum intensity that a TC can achieve in a given environment, it is expected to provide a useful guide to the statistical distribution of actual intensities achieved by real TCs (Sobel et al., 2016). Most TCs do not achieve their PI because of a variety of negative influences (e.g., vertical wind shear and ocean cooling effects).

We explore vertical wind shear, with weak vertical wind shear being favorable for hurricane convective organization and intensification (Merrill, 1988; Rios-Berrios & Torn, 2017). Vertical wind shear is calculated as the magnitude of the vector difference of wind velocity at 850 hPa and 200 hPa, computed from monthly-mean output. Increases in PI and decreases in vertical wind shear suggest an environment more conducive to future TC activity (Bister & Emanuel, 1998; Emanuel & Nolan, 2004; Emanuel, 2013).

2.3 Hydrodynamic-climatological modeling

Storm tide (combination of astronomical tide and storm surge) projections are based on simulations of Gori et al. (under review), using the 2D depth-integrated version of the hydrodynamic model ADvanced CIRCulation (ADCIRC) (Luettich et al., 1992; Westerink et al., 1994). We model storm tides for each of the eight CMIP6 models (herein

ADCIRC-CMIP6 models) that overlap with the study of Gori et al. (under review) (see Fig. 4 for the models) for the time periods and simulations employed in this study. TCs are modeled using the statistical-deterministic hurricane model developed by Emanuel et al. (2008) and Emanuel (2021). The ADCIRC mesh has a resolution of between 1 km nearshore and 100 km in the deep ocean (Marsooli et al., 2019; Lin et al., 2019; Gori et al., under review). Additionally, we focus only on synthetic TCs that pass within 200 km of NYC. Storm surges induced by TCs result in devastating flood events in NYC, as best exemplified by historical TCs such as Hurricane Donna in 1960 and Sandy in 2012. Following Lin et al. (2012), we assume the cyclone-threatened area for NYC to be within a 200-km radius from the Battery (74°W, 40.9°N; chosen as the representative location for NYC).

Previous work by Marsooli and Lin (2018) demonstrated that the impact of wave setup near NYC is relatively small; thus we do not include waves in our simulations. Statistical analysis is performed on the modeled peak storm tides to produce return period curves for each model. Flood return periods presented here are bias-corrected by comparing NCEP-based storm tide projections for the historical period with model-based projections on TC intensity for the same historical period and assuming the same bias in the future period. Assuming that the storms arrive as a stationary Poisson process under a given climate, the return period of TC-induced storm tide η_{TC} exceeding a given level h is (Marsooli et al., 2019):

$$\eta_{TC} = \frac{1}{Fr(1 - P\{\eta_T C \leq h\})} \tag{4}$$

where P$\{\eta_{TC} \leq$ h$\}$ is the cumulative probability distribution (CDF) of peak storm tide and Fr is the TC annual frequency. Here, we model the tail of the storm tide CDF using the Peaks-Over-Threshold method with a Generalized Pareto Distribution and maximum likelihood estimation (Coles, 2001). Non-parametric density estimations are used to model the rest of the distribution. We determine the tail threshold value by trial and error so that the smallest error in the distribution fitted to the tail is obtained.

3 Results

3.1 Future SLR and factors affecting TC activity

We present the CMIP6 ensemble mean relative SLR as a difference between years 1994–2014 of the historical simulation and years 2080–2100 of the SSP5-8.5 simulation (Fig. 1 a). GMSLR is 0.68 m, slightly larger than the AR6 estimate of 0.64 m (17th - 83rd percentile ranges of 0.52 - 0.83 m) in 2090 (Fox-Kemper et al., 2021), with projections across the ensemble positively correlated with GSAT change ($\rho = 0.82$; Fig. S4 a). Our ensemble estimates of GIC (0.16 m), thermal expansion (0.26 m) and GIS (0.1 m) (Fig. S5) are consistent with respectively values reported in AR6 of 0.15 m, 0.25 m and 0.1 m in 2090 (Fox-Kemper et al., 2021).

GMSLR projected here is higher than CMIP6 estimates presented in AR6 due predominately to the different methods used to project AIS contributions to GMSLR, with our results being 0.043 m higher (Fig. S5). In AR6, for processes in whose projections have at least medium confidence (with an assessed likelihood of 66-100%), projections for the AIS up to 2100 are estimated from a p-box that combines simulations from emulations of the Ice Sheet Model Intercomparison Project for CMIP6 (ISMIP6) (Edwards et al., 2021) and LARMIP-2 simulations (Levermann et al., 2020) augmented by AR5 surface mass balance model. ISMIP6 and LARMIP-2 projections in AR6 were estimated using CMIP6 GSAT distributions from a two-layer energy budget emulator (Fox-Kemper et al., 2021). Here, we utilize only the LARMIP-2 simulations (Levermann et al., 2020) augmented with two similar surface mass balance models to AR5. As noted in AR6, LARMIP-

2 median projections are higher than those of the ISMIP6 emulator, although AR6 could not distinguish which of ISMIP6 and LARMIP-2 is more realistic due to limitations in historical simulations and understanding of basal melting (Fox-Kemper et al., 2021).

21st century SLR scales with regional temperature change at approximately 0.15 and 0.14 m per degree in the western western North Atlantic and North West Pacific, respectively (Fig. 1 d,g; regions defined in Fig. 1 a). GMSLR also scales with GSAT change increase at an average rate of 0.11 m per degree across the ensemble. Relative SLR in the western North Atlantic and North West Pacific exceeds the global mean rate in part due to regionally high sterodynamic changes and as a consequence of the higher than global mean barystatic SLR associated with the spatial GRD fingerprints (Fig. S6 a-d). We note that future AIS contributions to SLR derived here will likely not scale with GSAT, as incorporating MISI and MICI in our AIS projections may further augment differences between models (Vega-Westhoff et al., 2020).

Whilst the CMIP6 ensemble mean June–November PI increases over most of the northern hemisphere tropics, there is a large region in the northern tropical Atlantic where the ensemble-mean PI decreases (Fig. 1 b). Projections of PI in CMIP3 (Vecchi & Soden, 2007a, 2007c) and CMIP5 models (Camargo, 2013; Sobel et al., 2016) have very similar patterns in the Northern Hemisphere to that shown here. In agreement with Vecchi and Soden (2007a, 2007c), we find that PI changes around the globe closely follow the structure of SST changes – with regions that warm more (less) than the tropical mean (relative SST; averaged over 35°S - 35°N) showing a PI increase (decrease) (Fig. 1 b). CMIP6 models project an average PI increase of 4.5% and 5.2% per degree regional temperature warming in the western North Atlantic and North West Pacific, respectively (Fig. 1 e,h). Globally averaged PI increases at a rate of 2.3 % per degree GSAT warming, consistent with an increase of 5% (likely range 1 to 10%) per two degrees warming as estimated in Knutson et al. (2020).

Using a subset of CMIP6 models, Hermans et al. (2021) found that global mean sea level (GMSL) scales with integrated GSAT, with most of the contributors to GMSL being more closely tied to time-integrated GSAT than instantaneous GSAT, meaning that sea level projections can only be interpreted if the warming levels are linked to a specific time-frame (Fox-Kemper et al., 2021). In contrast to GMSL, using a subset of CMIP6 models, we find that globally averaged PI appears to scale with instantaneous GSAT in a time- and scenario-independent manner (Fig. S7). Thus, the rates of increase in PI per degree GSAT change found here will likely be constant regardless of time or emissions scenario.

Basin-specific changes in vertical wind shear are projected, with increases across the tropical Atlantic and decreases across the northern tropical Pacific and western North Atlantic (Fig. 1 c). The CMIP6 model mean pattern is similar to that obtained in CMIP3 (Vecchi & Soden, 2007c) and CMIP5 (Camargo, 2013; Ting et al., 2019) models for the Northern Hemisphere TC season. These changes in vertical shear are associated to the projected decrease in the Pacific Walker circulation (Vecchi & Soden, 2007c), while the near-equatorial vertical shear weakening reflects a reduction of zonal overturning (Vecchi & Soden, 2007b, 2007c).

Projected changes to vertical wind shear over the ocean in the western North Atlantic and North West Pacific are -2.2 % and -2.7 % per degree regional temperature warming, respectively (Fig. 1 f,i). Reducing vertical wind shear in these regions is consistent with the expected expansion of the Hadley circulation (Lu et al., 2007; Kang & Lu, 2012), and the related northward shift of the midlatitude jet stream (Ting et al., 2019). To determine the change in vertical wind shear due to contributions from the upper and lower levels, Figure 2 shows the wind vector differences between the two periods. The intensification and northward shift of the midlatitude jet is clearly seen at both the upper and lower levels in the Atlantic and the Pacific, being stronger and more defined in models that project higher GSAT warming (Fig. 2 c,f). In agreement with a similar analysis of CMIP5 models (Ting et al., 2019), there is some indication of a southward flow at the lower level and northward flow at the upper level, implying an enhanced and northward extended Hadley circulation (Fig. 2 c,f).

Large inter-model differences exist: the CMIP6 model with the highest GSAT change (CanESM5; GSAT of 7.0°C) projects a GMSLR of 0.98 m and a 4% increase in globally averaged PI, whereas, the model with the lowest GSAT (CAMS-CSM1-0; GSAT of 2.8°C) projects a GMSLR of 0.61 m and an 8% increase in globally averaged PI (Fig. S4). Inter-model spread is strongly related to GSAT change, which is positively correlated to GM-SLR ($\rho = 0.82$) and globally averaged PI ($\rho = 0.62$; Fig. S4). Additionally, models fall roughly at the same position in the CMIP6 ensemble SLR and PI change distributions in the western North Atlantic when compared to the North West Pacific (e.g. CAMS-CSM1-0 projects the lowest average relative SLR and PI change in both regions; Fig. 1), suggesting that changes are coupled and are related by global mean changes.

Hence, in CMIP6 models, GMSLR and global mean PI change are closely related to GSAT change, whilst spatial patterns in PI change are tightly coupled with spatial changes in relative SST. Vertical wind shear tendencies are spatially more complex. In the western North Atlantic and North Pacific, vertical wind shear responds to changes in the mid-latitude jet, which is generally stronger in CMIP6 models that project higher GSAT change. As the climate system is strongly coupled, global and regional co-variability between SLR and TC activity, shown here to be related to GSAT change, may impose correlations between these variables. We next explore these correlations.

3.2 Correlation between SLR and large scale factors affecting TCs

The inter-model correlation is computed as the rank correlation across the CMIP6 ensemble between SLR and TC activity in historical and future (SSP5-8.5) simulations (Fig. 3). There are strong positive correlations between PI change and relative SLR in most regions: models with large PI increases show higher projected relative SLR (Figure 3 a). This strong SLR-PI relationship is consistent with both being broadly related to GSAT change (see Section 3.1). To explore the time periods and scenarios over which these correlations apply, we calculate intra-model correlations between relative SLR and PI change (Fig. S8). Intra-model correlations are calculated over the full 86 years of the SSP1-2.6, SSP2-4.5 and SSP5-8.5 scenarios for 11 CMIP6 models. The spatial patterns of intra-model correlations are very similar across scenarios, however, the correlation coefficients are stronger over time and in the higher emissions scenarios (Fig. S8). The reason for this difference may be due to larger ratio of forced signal to internal variability for later time period and for higher emissions scenarios. SLR contributions from land ice loss are strongly correlated with PI and vertical wind shear change in the western North Atlantic and North West Pacific (Fig. 3 e-j). SLR from land ice loss follows the spatial patterns of GRD fingerprints that is constant across models, meaning that the spatial correlations between TC activity and barystatic SLR are a result of common relations to global mean changes, rather than as a result of regional co-variability.

Relative SLR and vertical wind shear show regionally variable inter-model correlations (Fig. 3 b), that largely follows the spatial pattern of the ensemble mean vertical wind shear change (Fig. 1 c), being strongly negative in the western North Atlantic and North West Pacific, whilst positive in the tropical Atlantic region. Additionally, we find that PI and vertical wind shear are negatively correlated in parts of the western North Atlantic and North West Pacific (Fig. S9). The projected weakening of the vertical wind shear environment in the western North Atlantic and North West Pacific may help TCs reach their PI into the future. As PI and vertical wind shear are anti-correlated over much of the western North Atlantic and North West Pacific (Fig. S9), based solely on these metrics, we may well expect a non-linear increase in TC intensity.

The increases in PI across the western North Atlantic and North West Pacific, coupled with the more favorable vertical wind shear change suggests a large scale environment more conducive to TC intensification, with TCs having a better chance of achieving higher PIs in these regions (Ting et al., 2019). Additional and concurrent increases in relative SLR, suggest a significant and compounding intensification of flood hazard in these regions, based solely upon these metrics. For the Gulf Coast and tropical Atlantic, the future projected increase in vertical wind shear may induce a reduction of the intensity of strong landfalling TCs, although the increase in PI there may outweigh the effect of increasing vertical wind shear.

We have found strong inter- and intra-model correlations between SLR and TC activity change, with GSAT change being the key physical mechanism driving co-variability (Section. 3.1). The correlations between TC activity and relative SLR, may in turn affect the occurrence frequency and intensity of multivariate extreme events along the coast. We next explore the extent to which joint changes impact future coastal flood events at NYC.

3.3 Implications for Coastal Flooding at NYC

3.3.1 Future changes to the storm tide

Synthetic TCs used in this study are generated for the NYC area using the statistical-deterministic hurricane model of Emanuel et al. (2008) and Emanuel (2021). The TC model generates synthetic TCs for a given large-scale atmospheric and oceanic environment. Figure 4 presents the estimated storm surge return levels projected under the future climate, compared with those of the historical period (1994-2014), for NYC. In agreement with prior studies (Lin et al., 2012; Marsooli et al., 2019; Marsooli & Lin, 2020; Gori et al., under review), the storm tide level for a given return period substantially increases by the end of 21st century, due to relative SLR as well as TC climatology change. To quantify future flood hazard, we focus on the change in the 100-year storm tide level ($\Delta\eta_{100}$). Our projections show an increase of between 0.87 m and 2 m, with an average increase of 1.46 m (Fig. 4 j).

The increase in $\Delta\eta_{100}$ for each model at NYC is evidently related to each model's GSAT change and effective climate sensitivity (ECS) (Fig. 4 a-h and Table. 1). For example, changes to the $\Delta\eta_{100}$ for GFDL-ESM4 (GSAT = 3.6°C) is 0.87 m (TC only = 0.19 m; SLR only = 0.68 m). For CanESM5 (GSAT = 7.0°C) the projected increase is 1.7 m (TC only = 0.60 m; SLR only = 1.1 m) (Fig. 4 i). Importantly, relative SLR and TC climatology change generally both increase in a concurrent manner with GSAT change across models. A notable exception is EC-Earth3, which projects a large TC climatology increase, which can be attributed, in part, to a very large increase in TC frequency for this model (Table. 1). The difference in projected $\Delta\eta_{100}$ between the models with the lowest (GFDL-ESM4) and highest (CanESM5) projected GSAT change, incorporating each models own relative SLR and TC change, is 0.83 m at NYC by 2080-2100 (Fig. 4 i).

In our simulations, changes to storm frequency for NYC are large in the future (Table. 1). As TC frequency is a major uncertainty in the projections of TCs (Knutson et al., 2020), we repeat our analyses assuming that there is no change in annual frequency (Fig. 4 j and Fig. S10). By neglecting changes in TC frequency, projected TC storm surge changes are substantially reduced at NYC, with models that projected low GSAT change now projecting little change to TC storm tides (Fig. 4 k). We still, however, find evidence of concurrent increases in TC climatology with relative SLR and GSAT change at NYC. For example, CanESM5 projects an increase of $\Delta\eta_{100}$ of 1.27 m (TC only = 0.17 m; SLR only = 1.1 m), whilst GFDL-ESM4 projects an increase to the $\Delta\eta_{100}$ of 0.7 m (TC only = 0.019 m; SLR only = 0.68 m). Changing storm tide levels driven by TC climatology change suggest that TC intensity, track, size and translation speed could change by the end of 21st century. We next explore these metrics.

3.3.2 Changing TC characteristics

We find that the TC track exhibits little variability along the US East Coast into the future (Fig. 5 a and Fig. S11 a-h). In contrast to our results, the downscaling model of Garner et al. (2017) projected using three CMIP5 models that climate change impacts on TC, apart from SLR, has little net influence on storm surge hazard in the region by 2100, as TC tracks shifted away from landfall in the region under climate change, which offset the effect of storm strengthening. We note that MIROC6 exhibits a similar track shift to that found in Garner et al. (2017) (Fig. S11 b) and little change in very low probability surge heights (Fig. 4 b).

The movement of TCs tracks, is predominately determined by the steering winds, with modifications due to the beta effect (Chan, 2005), the former being strongly related to the position and strength of the subtropical highs. In general agreement with CMIP3 (26 models in Li et al. (2012)) and CMIP5 models (13 models in Li et al. (2013) and 20 models in Camargo (2013)), we find a significant intensification of the North Atlantic subtropical high (Fig. 5 b-c and Fig. S11 i-p), which has been related to an increase in thermal contrast between the land and ocean (Li et al., 2012). CMIP6 models mean sea-level pressure (SLP) differences indicate that future SLP is significantly higher (100 Pa) over the North Atlantic Ocean and lower over the United States (Fig. 5 b-c and Fig. S11 i-p). Additionally, mean SLP differences of all 26 CMIP6 models suggest a more westward pattern in the North Atlantic subtropical high compared to the ADCIRC-CMIP6 subset (Fig. 5 c). These changes in SLP support our finding that the tracks of TCs that affect NYC will not be substantially shifted away from the coast into the future.

The flooding potential, and to some extent the wind damage, caused by TCs can be strongly affected by their translation speed. Slower TCs allow winds to blow onshore for longer periods of time, resulting in possibly larger and longer coastal flooding. Our analysis of TC translation speed and intensity (maximum wind speed) also reveals an increase in the number of slow-moving and stronger TCs along the US East Coast (Fig. 6 a-b and Fig. S12-13). At NYC, models that project higher GSAT change and relative SLR, project considerably slower and more intense TCs than low GSAT change models (Table. 1). For example, synthetic TCs derived from CanESM5 suggest changes to TC intensity and translation speed of 25% and -29% respectively, whilst GFDL-ESM4 projects changes of 7.6% and -5.9% (Table. 1).

We utilize the complete wind profile of Chavas et al. (2015) to estimate the radius of maximum wind speed, where projected decreases in radius of maximum wind speed are consistent with increases in maximum wind speed, assuming constant TC outer sizes (Chavas et al., 2016; Knutson et al., 2015). As TC intensity is projected to increase, we find that the radius of maximum wind speed also decreases along the US East Coast (Fig. 6 c and Fig. S14). With progressive warming, TCs may therefore have smaller radius of maximum wind speed, which may act to counteract storm surge increases driven by stronger and slower moving TCs.

We also explore inter-model correlations between relative SLR and projected changes in TC characteristics (Fig. 6 d-f). Relative SLR is positively correlated with TC intensity, and negatively correlated with translation speed and radius of maximum wind speed in the NYC region. Based on these correlations, we can deduce that compounding of increased flood hazard at NYC with relative SLR and GSAT warming will likely be driven by stronger and slowing moving TCs and possibly their increased frequency, that may be counteracted in part by TCs with smaller radius of maximum wind speed.

3.3.3 Implications for coastal flood modeling

We have found that relative sea levels and TC storm surges both increase strongly with GSAT warming at NYC. In this section, we evaluate (1) the extent to which studies misrepresent future flood hazard by assuming independence conditional on the emissions scenario and (2) the impact of model selection bias on projected changes to flood hazard. To explore (1), we calculate the flood hazard through the convolution of the distributions of storm tide and SLR, assuming they are statistically independent (Marsooli et al., 2019). We compare the ADCRIC-CMIP6 projection that includes correlated changes (dark blue bars on Fig. 4 i-j) with the ADCRIC-CMIP6 projection obtained through convolution (light blue bars on Fig. 4 i-j). We find that by neglecting positive correlation between SLR and TC surge change, the projection of $\Delta\eta_{100}$ is under-estimated by 0.08 m (6%) and 0.05 m (5%) assuming frequency changes and no frequency change, respectively.

Inter-model differences in relative SLR and TC change indicate that selection bias may substantially alter the projected change in flood hazard at NYC. For example, the ADCIRC-CMIP6 models are negatively skewed in GSAT projections compared to the distribution of all 26 CMIP6 models (three are in the top 25%; Fig. S1 b), which may be leading to overly strong projections of compound changes at NYC. To explore potential selection bias, we compare the ADCRIC-CMIP6 projection that includes correlated changes (dark blue bars; Fig. 4 i-j) with a simple scaling relationship between ADCRIC-CMIP6 TC climatology change and GSAT change, that is applied to the projections of all 26 CMIP6 models (green bars on Fig. 4 i-j). At NYC the $\Delta\eta_{100}$ due to TC climatology change increases at a rate of 0.10 m (lowest 0.06 m; highest 0.15 m) and 0.02 m (lowest 0.008 m; highest 0.032 m) per degree GSAT change assuming frequency changes and no frequency change, respectively (Fig. S15 a,d). We apply these scaling relationships to the GSAT and relative SLR projections of all 26 CMIP6 models (Fig. S15 b-c,e-f). Specifically, we randomly sample one of the eight scaling factors (from the eight ADCIRC-CMIP6 models) and apply it to a randomly selected one of the 26 CMIP6 models based on its GSAT and add its SLR projection 100,000 times.

By comparing this scaling estimate with the ADCRIC-CMIP6 projection that includes correlated changes, we find that selection bias is leading to an over-estimated average projection of $\Delta\eta_{100}$ of 0.08 m (5%) and 0.03 m (3%) assuming frequency changes and no frequency change, respectively (Fig. 4 i-j). By comparing the average scaling estimate that includes correlation (dark green bars on Fig. 4 i-j) with the scaling estimate that doesn't include correlation (light green bars on Fig. 4 i-j), we also find that the average is under-estimated by 0.09 m (7%) and 0.06 m (6%) assuming frequency changes and no frequency change, respectively (Fig. 4 i-j). Additionally, the range is under-estimated by 0.17 m (11%) and 0.05 m (5%) when the positive correlation are neglected, assuming frequency change and no frequency change, respectively (Fig. 4 i-j).

We have found that by focusing on a subset of AOGCMs that do not reflect the full distribution of GSAT changes within the emission scenario, and by assuming independence between SLR and storm tide change, coastal flood hazard assessments may not accurately capture future coastal flood hazard. We recommend that future studies that focus on a specific emissions scenario: (1) construct SLR and TC projections inherent to each model to ensure that correlations are incorporated, (2) be mindful of the GSAT change and ECS of each CMIP6 model used, as selection bias may substantially alter flood hazard projections and (3) consider extremes as well as average projections, given that model variation is reduced when the correlation between SLR and TC projections are neglected.

4 Discussion

The results of this analysis indicate that flood hazard in the western North Atlantic and North West Pacific will increase substantially over the twenty first century due to relative SLR, compounded by TC climatology change. As shown in Marsooli et al. (2019), the effect of TC climatology change is likely to be larger than the effect of SLR for over 40% of coastal counties in the Gulf of Mexico. Additionally, the relative effect of TC climatology change increased continuously from New England, mid-Atlantic, southeast Atlantic, to the Gulf of Mexico. Effects on flooding of positive correlations between relative SLR and TC climatology found here, may therefore exhibit substantial spatial and temporal heterogeneity. For NYC, where SLR is considerably larger than projected TC surge change (see Section 3.3), neglecting correlated changes results in the average projected change to the historical 100-year flood level being under-estimated by 0.09 m (7%) and 0.06 m (6% of change) assuming frequency changes and no frequency changes, respectively. In some lower latitude regions that have higher projected TC climatology change compared to NYC (Marsooli et al., 2019), such as along the Gulf of Mexico and in parts of the western Pacific, neglecting positive correlations may lead to higher under-estimation of coastal flood hazard.

We also treat storm surge and SLR as linearly additive. This is problematic because interactions between SLR and surge and tides can potentially create a bias, up to the order of 15% in the future flood elevation, either high or low depending on exact geographic location (Resio & Irish, 2015). However, future SLR-TC interactions are expected to be small at NYC (Lin et al., 2012, 2010). Correlations between SLR and TC storm surge may also impact SLR-TC surge interactions; if changes to both SLR and TC storm surges are large then interactions between these components may also be stronger, further impacting future flood hazard. The spatial and temporal variability in correlations should be explored in future studies.

SLR and future TC activity will respond to radiative forcing, atmospheric feedbacks, the horizontal and vertical distribution of oceanic and atmospheric warming, and changes in climate oscillations, amongst others (Woodruff et al., 2013; Little et al., 2015). As the climate is a strongly coupled system, regional changes in climate forcing may be co-dependent (Lambert et al., 2021); and it is this co-dependence that imposes correlations between SLR and TC activity and associated coastal flooding. In this analysis, we do not attempt to rigorously explain correlations across the ensemble, as an individual model's response may be a combination of multiple drivers that have not been considered here. More efforts to clarify causal mechanisms and role of uncertainties are required to constrain the timescales and radiative forcing scenarios over which these correlations apply.

We also note that our results may be influenced by model selection bias, resulting from the fact that not all model output is available. To explore this, we compare GSAT projections of models used this study (26 models) to all available CMIP6 models that have surface temperature (tas) for the simulations and run used (34 in total; Fig. S1 c). The 26 CMIP6 models used here, span the full range of projected GSAT change, giving us some confidence that our results should be largely unaffected by the addition of other CMIP6 models. In addition, our results rely on a number of land ice SLR parameterizations that have considerable uncertainty. Ideally, our methodology would be applied to explicit model projections of all sea-level components, rather than parameterizations.

As the inter-model spread contributes a large fraction of the total projection uncertainty in SLR and TC activity, uncertainties may be reduced if outlier models can be shown to be unreliable (Little et al., 2015). In particular, our results indicate that the divergent behaviour of CMIP6 models in projections of future TC activity and relative SLR, is driven by models that project high ECS. Some high ECS models used in this study project more positive cloud feedback in response to increasing green-house gases, and they also tend to have a stronger cooling effect from aerosol-cloud interactions (ACI) when compared to low ECS models (Wang et al., 2021). These strong effects in the high ECS models offset each other during much of the 20th century, when both anthropogenic aerosols and emissions increased. However, these high ECS models poorly simulate the spatial pattern of historical warming compared to low ECS models as aerosols are concentrated in the Northern Hemisphere (Wang et al., 2021).

The compensating affects of strong ACI and cloud feedback in the high ECS models, which occurs over the historical period, does not occur into the future, as aerosols are projected to decrease as greenhouse gases rise. CMIP6 models with more positive cloud feedback, as a result, tend to have higher 21st century projected warming (Brunner et al., 2020), ECS (Wang et al., 2021), and therefore, potentially higher SLR and future TC activity. Indeed, we find that CMIP6 models that project the highest GMSLR and globally averaged PI in this study also project the highest ECS and strongest cloud feedback (Fig. S16). If these high ECS and cloud-feedback models, which poorly simulate the spatial pattern of historical warming, can be shown to be unrealistic, substantial uncertainty reductions in projections (that are derived directly from CMIP6 models) of TC activity and SLR, could result.

Finally, rain rates near the centres of TCs are also expected to increase with increasing global temperatures (Knutson et al., 2015, 2020). The amount of TC related rainfall that any given local area will experience is proportional to the rain rates and inversely proportional to the translation speeds of TCs (Kossin, 2018). Our projections of slower moving storms along the US East Coast may therefore contribute to an increased rate of rain in TCs in some regions (Gori et al., under review). In the northeast region of the United States, especially in New England, coastal flooding induced by extra-tropical cyclones (ETCs) are more frequent (but less destructive) than TC-induced flooding (Booth et al., 2016). The effect of climate change on ETC storm surges is thought to be relatively small on average along the US East Coast, although large uncertainties exist among climate models (Lin et al., 2019). It is likely that correlations between relative SLR and TC precipitation and ETC activity may well impact future flood hazard in some regions.

5 Conclusion

The results of this analysis indicate that relative SLR is correlated with aspects of TC activity over much of the western North Atlantic and North West Pacific, suggesting that progressive warming will compound future flood hazard in these regions. Increases in PI, coupled with more favorable vertical wind shear also suggest a large scale environment more conducive to TCs in these regions. Based on analyses of synthetic TCs and hydrodynamic modeling, we find that large scale co-variability substantially impacts local flood hazard at NYC, with future storm tides predicted to increase with warming due to relative SLR coupled with progressively stronger and slower moving TCs along the US East Coast, even if TC frequency remain unchanged.

We have found that by focusing on a subset of AOGCMs that do not reflect the full distribution of GSAT changes within the emission scenario, and by assuming independence between SLR and storm tide change, coastal flood hazard assessments may not accurately capture future coastal flood hazard. By neglecting correlated changes, the average and range of projected change to the historical 100-year flood level is under-estimated by 0.09 m (7%) and 0.17 m (11%), respectively. We recommend that future studies that focus on a specific emissions scenario: (1) construct SLR and TC projections inherent to each model to ensure that correlations are incorporated, (2) be mindful of the GSAT change and ECS of each CMIP6 model used, as selection bias may substantially alter flood hazard projections and (3) consider extremes as well as average projections, given that model variation is reduced when the correlation between SLR and TC projections are neglected.

Our paper is novel in that we explore global scale correlations between TC activity and relative SLR that includes contributions from land ice loss and associated GRD fingerprints and from non-climatic changes. We also conduct climatology-hydrodynamic modeling to quantify the impact of correlations on future flood hazard and explore correlations between SLR and synthetic TCs. We show that aspects of TC activity change are likely to co-vary with relative SLR, meaning that flood hazard assessments that neglect the joint influence of these factors will misrepresent future flood hazard. We recommend that future studies on coastal flood hazards explore correlated changes between future TCs, ETCs, precipitation and relative SLR.

Acknowledgments

We are grateful to D.J Rasmussen who provided helpful comments on the manuscript. The authors thank T. Frederikse for providing output from the GRD model. JWL was supported by the Princeton University Fellowship in Natural Sciences and Engineering. REK was supported by NSF award ICER-1663807, NASA award 80NSSC20K1724, and NASA JPL project 105393.509496.02.08.13.31. NL was supported by NSF award 1652448. CMIP6 data is available from `https://esgf-node.llnl.gov/projects/cmip6/`. Output from ADCIRC modeling is available from the authors upon reasonable request. Code used in this analysis can be obtained at `https://github.com/JWLockwood/Lockwoodetal2021_Physdependence.git`.

References

Argus, D., Peltier, W., Drummond, R., & Moore, A. (2014, 05). The antarctica component of postglacial rebound model ice-6gc (vm5a) based on gps positioning, exposure age dating of ice thicknesses, and relative sea level histories. *Geophysical Journal International*, *198*, 537-563. doi: 10.1093/gji/ggu140

Aschwanden, A., Fahnestock, M. A., Truffer, M., Brinkerhoff, D. J., Hock, R., Khroulev, C., ... Khan, S. A. (2019). Contribution of the greenland ice sheet to sea level over the next millennium. *Science Advances*, *5*(6), eaav9396. doi: 10.1126/sciadv.aav9396

Bamber, J. L., Oppenheimer, M., Kopp, R. E., Aspinall, W. P., & Cooke, R. M. (2019). Ice sheet contributions to future sea-level rise from structured expert judgment. , *116*(23). doi: 10.1073/pnas.1817205116

Bhatia, K., Vecchi, G., Murakami, H., Underwood, S., & Kossin, J. (2018). Projected response of tropical cyclone intensity and intensification in a global climate model. *Journal of Climate*, *31*(20), 8281–8303. doi: 10.1175/JCLI-D-17-0898.1

Bilskie, M. V., Hagen, S. C., Alizad, K., Medeiros, S. C., Passeri, D. L., Needham, H. F., & Cox, A. (2016). Dynamic simulation and numerical analysis of hurricane storm surge under sea level rise with geomorphologic changes along the northern gulf of mexico. *Earth's Future*, *4*(5), 177-193. Retrieved from `https://agupubs.onlinelibrary.wiley.com/doi/abs/10.1002/2015EF000347` doi: https://doi.org/10.1002/2015EF000347

Bilskie, M. V., Hagen, S. C., Medeiros, S. C., & Passeri, D. L. (2014). Dynamics of sea level rise and coastal flooding on a changing landscape. *Geophysical Research Letters*, *41*(3), 927-934. Retrieved from `https://agupubs.onlinelibrary.wiley.com/doi/abs/10.1002/2013GL058759` doi: https://doi.org/10.1002/2013GL058759

Bister, M., & Emanuel, K. A. (1998). Dissipative heating and hurricane intensity. *Meteorology and Atmospheric Physics*, *65*(3-4), 233–240. doi: 10.1007/BF01030791

Booth, J., Rieder, H., & Kushnir, Y. (2016, 09). Comparing hurricane and extratropical storm surge for the mid-atlantic and northeast coast of the united states for 1979–2013. *Environmental Research Letters*, *11*, 094004. doi: 10.1088/1748-9326/11/9/094004

Brunner, L., Pendergrass, A. G., Lehner, F., Merrifield, A. L., Lorenz, R., & Knutti, R. (2020). Reduced global warming from cmip6 projections when weighting models by performance and independence. *Earth System Dynamics*, *11*(4), 995–1012. Retrieved from `https://esd.copernicus.org/articles/11/995/2020/` doi: 10.5194/esd-11-995-2020

Buchanan, M., Kopp, R., Oppenheimer, M., & Tebaldi, C. (2016, August 1). Allowances for evolving coastal flood risk under uncertain local sea-level rise. *Climatic Change*, *137*(3-4), 347–362. doi: 10.1007/s10584-016-1664-7

Camargo, S. J. (2013). Global and regional aspects of tropical cyclone activity in the CMIP5 models. *Journal of Climate*, *26*(24), 9880–9902. doi: 10.1175/JCLI-D-12-00549.1

Camargo, S. J., & Wing, A. A. (2021). Increased tropical cyclone risk to coasts. *Science*, *371*(6528), 458–459. doi: 10.1126/science.abg3651

Chan, J. C. (2005). The physics of tropical cyclone motion. *Annual Review of Fluid Mechanics*, *37*(1), 99-128. doi: 10.1146/annurev.fluid.37.061903.175702

Chavas, D. R., Lin, N., & Emanuel, K. (2015). A model for the complete radial structure of the tropical cyclone wind field. part i: Comparison with observed structure. *Journal of the Atmospheric Sciences*, *72*(9), 3647 - 3662. Retrieved from `https://journals.ametsoc.org/view/journals/atsc/72/9/jas-d-15-0014.1.xml` doi: 10.1175/JAS-D-15-0014.1

Chavas, D. R., Lin, N., & Emanuel, K. (2016). A model for the complete radial structure of the tropical cyclone wind field . part ii : Wind field variability. *Journal of the Atmospheric Sciences*, *72*(9). doi: 10.1175/JAS-D-15-0185.1

Church, J., Clark, P., Cazenave, A., Gregory, J., Jevrejeva, S., Levermann, A., ... Alakkat, U. (2013, 01). Climate change 2013: The physical science basis. contribution of working group i to the fifth assessment report of the intergovernmental panel on climate change. *Sea Level Change*, 1138-1191.

Coles, S. (2001). An introduction to statistical modeling of extreme values.

Cook, J. M., Tedstone, A. J., Williamson, C., McCutcheon, J., Hodson, A. J., Dayal, A., ... Tranter, M. (2020). Glacier algae accelerate melt rates on the south-western greenland ice sheet. *The Cryosphere*, *14*(1), 309–330. Retrieved from `https://tc.copernicus.org/articles/14/309/2020/` doi: 10.5194/tc-14-309-2020

De Dominicis, M., Wolf, J., Jevrejeva, S., Zheng, P., & Hu, Z. (2020). Future Interactions Between Sea Level Rise, Tides, and Storm Surges in the World's Largest Urban Area. *Geophysical Research Letters*, *47*(4). doi: 10.1029/2020GL087002

Delhasse, A., Fettweis, X., Kittel, C., Amory, C., & Agosta, C. (2018). Brief communication: Impact of the recent atmospheric circulation change in summer on the future surface mass balance of the greenland ice sheet. *The Cryosphere*, *12*(11), 3409–3418. Retrieved from `https://tc.copernicus.org/articles/12/3409/2018/` doi: 10.5194/tc-12-3409-2018

Edwards, T. L., Nowicki, S., Marzeion, B., Hock, R., Goelzer, H., Seroussi, H., ... Zwinger, T. (2021). Projected land ice contributions to 21st century sea level rise. *Nature*, *593*, 74–82. doi: 10.1038/s41586-021-03302-y

Emanuel. (2013). Downscaling CMIP5 climate models shows increased tropical cyclone activity over the 21st century. *Proceedings of the National Academy of Sciences of the United States of America*, *110*(30), 12219–12224. doi: 10.1073/pnas.1301293110

Emanuel. (2021). Response of global tropical cyclone activity to increasing co2: Results from downscaling cmip6 models. *Journal of Climate*, *34*, 57-70.

Emanuel, & Nolan, D. S. (2004). Tropical cyclone activity and the global climate system. *26th Conference on Hurricanes and Tropical Meteorology*(August), 240–241.

Emanuel, Sundararajan, R., & Williams, J. (2008, mar). Hurricanes and Global Warming: Results from Downscaling IPCC AR4 Simulations. *Bulletin of the American Meteorological Society*, *89*(3), 347–368. Retrieved from `https://doi.org/10.1175/BAMS-89-3-347` doi: 10.1175/BAMS-89-3-347

Eyring, V., Bony, S., Meehl, G. A., Senior, C. A., Stevens, B., Stouffer, R. J., & Taylor, K. E. (2016). Overview of the coupled model intercomparison project phase 6 (cmip6) experimental design and organization. *Geoscientific Model Development*, *9*(5), 1937–1958. Retrieved from `https://gmd.copernicus.org/articles/9/1937/2016/` doi: 10.5194/gmd-9-1937-2016

Farinotti, D., Huss, M., Fürst, J., Landmann, J., Machguth, H., Maussion, F., & Pandit, A. (2019, 03). A consensus estimate for the ice thickness distribution of all glaciers on earth. *Nature Geoscience*, *12*. doi: 10.1038/s41561-019-0300-3

Fox-Kemper, B., Hewitt, H. T., Xiao, C., Aalgeirsdóttir, G., Drijfhout, S. S., Edwards, T. L., ... Yu, Y. (2021). Ocean, cryosphere and sea level change. in: Climate change 2021: The physical science basis. contribution of working group i to the sixth assessment report of the intergovernmental panel on climate change. *Cambridge University Press.*.

Frederikse, T., Buchanan, M. K., Lambert, E., Kopp, R. E., Oppenheimer, M., Rasmussen, D. J., & de Wal, R. S. (2020). Antarctic Ice Sheet and emission scenario controls on 21st-century extreme sea-level changes. *Nature Communications*, *11*(1), 1–11. Retrieved from `http://dx.doi.org/10.1038/`

s41467-019-14049-6 doi: 10.1038/s41467-019-14049-6
Fürst, J. J., Goelzer, H., & Huybrechts, P. (2015). Ice-dynamic projections of the greenland ice sheet in response to atmospheric and oceanic warming. *The Cryosphere*, *9*(3), 1039–1062. Retrieved from https://tc.copernicus.org/articles/9/1039/2015/ doi: 10.5194/tc-9-1039-2015
Garner, A. J., Mann, M. E., Emanuel, K. A., Kopp, R. E., Lin, N., Alley, R. B., ... Pollard, D. (2017). Impact of climate change on new york city's coastal flood hazard: Increasing flood heights from the preindustrial to 2300 ce. *Proceedings of the National Academy of Sciences*, *114*(45), 11861–11866. Retrieved from https://www.pnas.org/content/114/45/11861 doi: 10.1073/pnas.1703568114
Genthon, C., Krinner, G., & Castebrunet, H. (2009). Antarctic precipitation and climate-change predictions: horizontal resolution and margin vs plateau issues. *Annals of Glaciology*, *50*(50), 55–60. doi: 10.3189/172756409787769681
Gori, A., Lin, N., Xi, D., , & Emanuel, K. (under review). Tropical cyclone climatology change greatly exacerbates us joint rainfall-surge hazard. *Nature Climate Change*.
Gregory, Griffies, S. M., Hughes, C. W., Lowe, J. A., Church, J. A., Fukimori, I., ... Tamisiea, M. E. (2019). *Concepts and Terminology for Sea Level : Mean , Variability and Change , Both Local and Global* (Vol. 0123456789). doi: 10.1007/s10712-019-09525-z
Gregory, & Huybrechts, P. (2006). Ice-sheet contributions to future sea-level change. *Philosophical Transactions of the Royal Society A: Mathematical, Physical and Engineering Sciences*, *364*(1844), 1709-1732. doi: 10.1098/rsta.2006.1796
Griffies, S. M., Danabasoglu, G., Durack, P. J., Adcroft, A. J., Balaji, V., Böning, C. W., ... Yeager, S. G. (2016). OMIP contribution to CMIP6: Experimental and diagnostic protocol for the physical component of the Ocean Model Intercomparison Project. *Geoscientific Model Development*, *9*(9), 3231–3296. doi: 10.5194/gmd-9-3231-2016
Griffies, S. M., & Greatbatch, R. J. (2012). Physical processes that impact the evolution of global mean sea level in ocean climate models. *Ocean Modelling*, *51*, 37–72. Retrieved from http://dx.doi.org/10.1016/j.ocemod.2012.04.003 doi: 10.1016/j.ocemod.2012.04.003
Griffies, S. M., Yin, J., Durack, P. J., Goddard, P., Bates, S. C., Behrens, E., ... Zhang, X. (2014). An assessment of global and regional sea level for years 1993-2007 in a suite of interannual core-II simulations. *Ocean Modelling*, *78*, 35–89. Retrieved from http://dx.doi.org/10.1016/j.ocemod.2014.03.004 doi: 10.1016/j.ocemod.2014.03.004
Hausfather, Z., & Peters, G. P. (2020). Heading in here running to two lines. *Nature*.
Hermans, T. H. J., Gregory, J. M., Palmer, M. D., Ringer, M. A., Katsman, C. A., & Slangen, A. B. A. (2021). Projecting global mean sea-level change using cmip6 models. *Geophysical Research Letters*, *48*(5), e2020GL092064. Retrieved from https://agupubs.onlinelibrary.wiley.com/doi/abs/10.1029/2020GL092064 (e2020GL092064 2020GL092064) doi: https://doi.org/10.1029/2020GL092064
Hock, R., Bliss, A., MARZEION, B., GIESEN, R. H., HIRABAYASHI, Y., HUSS, M., ... SLANGEN, A. B. A. (2019). Glaciermip – a model intercomparison of global-scale glacier mass-balance models and projections. *Journal of Glaciology*, *65*(251), 453–467. doi: 10.1017/jog.2019.22
Hofer, S., Tedstone, A., Fettweis, X., & Bamber, J. (2019, 07). Cloud microphysics and circulation anomalies control differences in future greenland melt. *Nature Climate Change*, *9*, 523. doi: 10.1038/s41558-019-0507-8
Hunter, J. (2011, 11). A simple technique for estimating an allowance for uncertain sea-level rise. *Climatic Change*, *113*. doi: 10.1007/s10584-011-0332-1

Idier, D., Bertin, X., Thompson, P., & Pickering, M. D. (2019). Interactions Between Mean Sea Level, Tide, Surge, Waves and Flooding: Mechanisms and Contributions to Sea Level Variations at the Coast. *Surveys in Geophysics*, *40*(6), 1603–1630. Retrieved from https://doi.org/10.1007/s10712-019-09549-5 doi: 10.1007/s10712-019-09549-5

Joughin, I., Smith, B., & Medley, B. (2014, 05). Marine ice sheet collapse potentially under way for the thwaites glacier basin, west antarctica. *Science (New York, N.Y.)*, *344*. doi: 10.1126/science.1249055

Kang, S. M., & Lu, J. (2012). Expansion of the hadley cell under global warming: Winter versus summer. *Journal of Climate*, *25*(24), 8387 - 8393. Retrieved from https://journals.ametsoc.org/view/journals/clim/25/24/jcli-d-12-00323.1.xml doi: 10.1175/JCLI-D-12-00323.1

Khan, S., Bjørk, A., Bamber, J., Morlighem, M., Bevis, M., Kjær, K., … Schenk, T. (2020, 11). Centennial response of greenland's three largest outlet glaciers. *Nature Communications*, *11*. doi: 10.1038/s41467-020-19580-5

Kirezci, E., Young, I., Ranasinghe, R., Muis, S., Nicholls, R., Lincke, D., & Hinkel, J. (2020, 07). Projections of global-scale extreme sea levels and resulting episodic coastal flooding over the 21st century. *Scientific Reports*, *10*, 11629. doi: 10.1038/s41598-020-67736-6

Kittel, C., Amory, C., Agosta, C., Jourdain, N. C., Hofer, S., Delhasse, A., … Fettweis, X. (2021). Diverging future surface mass balance between the Antarctic ice shelves and grounded ice sheet. , 1215–1236.

Knutson, Camargo, S. J., Chan, J. C. L., Emanuel, K., Ho, C.-H., Kossin, J., … Wu, L. (2020). Tropical Cyclones and Climate Change Assessment: Part II: Projected Response to Anthropogenic Warming. *Bulletin of the American Meteorological Society*, *101*(3), E303–E322. Retrieved from https://doi.org/10.1175/BAMS-D-18-0194.1 doi: 10.1175/BAMS-D-18-0194.1

Knutson, Sirutis, J., Zhao, M., Tuleya, R., Bender, M., Vecchi, G., … Chavas, D. (2015). Global projections of intense tropical cyclone activity for the late twenty-first century from dynamical downscaling of cmip5/rcp4.5 scenarios. *Journal of Climate*, *28*, 7203-7224.

Kopp, R. E., Deconto, R. M., Bader, D. A., Hay, C. C., Radley, M., Kulp, S., … Strauss, B. H. (2017). Earth ' s Future Evolving Understanding of Antarctic Ice-Sheet Physics and Ambiguity in Probabilistic Sea-Level Projections Earth ' s Future.

Kopp, R. E., Hay, C. C., Little, C. M., & Mitrovica, J. X. (2015). Geographic Variability of Sea-Level Change. *Current Climate Change Reports*, *1*(3), 192–204. doi: 10.1007/s40641-015-0015-5

Kopp, R. E., Horton, R. M., Little, C. M., Mitrovica, J. X., Oppenheimer, M., Rasmussen, D. J., … Tebaldi, C. (2014). Earth ' s Future Probabilistic 21st and 22nd century sea-level projections at a global network of tide-gauge sites Earth ' s Future. , 383–407. doi: 10.1002/2014EF000239.Abstract

Kossin, J. P. (2018, June). A global slowdown of tropical-cyclone translation speed. *Nature*, *558*(7708), 104—107. Retrieved from https://doi.org/10.1038/s41586-018-0158-3 doi: 10.1038/s41586-018-0158-3

Lambert, E., Le Bars, D., Goelzer, H., & van de Wal, R. S. (2021). Correlations between sea-level components are driven by regional climate change. *Earth's Future*, *9*(2), e2020EF001825. Retrieved from https://agupubs.onlinelibrary.wiley.com/doi/abs/10.1029/2020EF001825 (e2020EF001825 2020EF001825) doi: https://doi.org/10.1029/2020EF001825

Levermann, A., Winkelmann, R., Albrecht, T., Goelzer, H., Golledge, N. R., Greve, R., … Van De Wal, R. S. (2020). Projecting Antarctica's contribution to future sea level rise from basal ice shelf melt using linear response functions of 16 ice sheet models (LARMIP-2). *Earth System Dynamics*, *11*(1), 35–76. doi: 10.5194/esd-11-35-2020

Li, Li, L., Ting, M., & Liu, Y. (2012, 09). Intensification of northern hemisphere near-surface subtropical highs in a warming climate. *Nature Geoscience*. doi: 10.1038/ngeo1590

Li, Sun, C., & Jin, F.-F. (2013). Nao implicated as a predictor of northern hemisphere mean temperature multidecadal variability. *Geophysical Research Letters*, *40*(20), 5497-5502. doi: https://doi.org/10.1002/2013GL057877

Lin, N., Emanuel, K., Oppenheimer, M., & Vanmarcke, E. (2012). Physically based assessment of hurricane surge threat under climate change. *Nature Climate Change*, *2*, 462-467. doi: 10.1038/nclimate1389

Lin, N., Emanuel, K. A., Smith, J. A., & Vanmarcke, E. (2010). Risk assessment of hurricane storm surge for new york city. *Journal of Geophysical Research: Atmospheres*, *115*(D18). doi: https://doi.org/10.1029/2009JD013630

Lin, N., Kopp, R. E., Horton, B. P., & Donnelly, J. P. (2016). Hurricane sandy's flood frequency increasing from year 1800 to 2100. *Proceedings of the National Academy of Sciences*, *113*(43), 12071–12075. Retrieved from https://www.pnas.org/content/113/43/12071 doi: 10.1073/pnas.1604386113

Lin, N., Marsooli, R., & Colle, B. (2019, 05). Storm surge return levels induced by mid-to-late-twenty-first-century extratropical cyclones in the northeastern united states. *Climatic Change*, *154*. doi: 10.1007/s10584-019-02431-8

Little, Horton, R. M., Kopp, R. E., Oppenheimer, M., Vecchi, G. A., & Villarini, G. (2015). Joint projections of US East Coast sea level and storm surge. *Nature Climate Change*, *5*(12), 1114–1120. doi: 10.1038/nclimate2801

Liu, Y., Asher, T. G., & Irish, J. L. (2019). Physical drivers of changes in probabilistic surge hazard under sea level rise. *Earth's Future*, *7*(7), 819-832. Retrieved from https://agupubs.onlinelibrary.wiley.com/doi/abs/10.1029/2019EF001216 doi: https://doi.org/10.1029/2019EF001216

Lu, J., Vecchi, G. A., & Reichler, T. (2007). Expansion of the hadley cell under global warming. *Geophysical Research Letters*, *34*(6).

Luettich, R., Jr, Westerink, J., & Scheffner, N. (1992, 11). Adcirc: An advanced three-dimensional circulation model for shelves, coasts, and estuaries. report 1. theory and methodology of adcirc-2ddi and adcirc-3dl. *Dredging Research Program Tech. Rep. DRP-92-6*, 143.

Marsooli, R., & Lin, N. (2018). Numerical modeling of historical storm tides and waves and their interactions along the U.S. East and Gulf Coasts. *Journal of Geophysical Research: Oceans*, *123*(5), 3844–3874. doi: 10.1029/2017JC013434

Marsooli, R., & Lin, N. (2020, 12). Impacts of climate change on hurricane flood hazards in jamaica bay, new york. *Climatic Change*, *163*, 1-19. doi: 10.1007/s10584-020-02932-x

Marsooli, R., Lin, N., Emanuel, K., & Feng, K. (2019). Climate change exacerbates hurricane flood hazards along US Atlantic and Gulf Coasts in spatially varying patterns. *Nature Communications*, *10*(1), 1–9. Retrieved from http://dx.doi.org/10.1038/s41467-019-11755-z doi: 10.1038/s41467-019-11755-z

Marzeion, B., Hock, R., Anderson, B., Bliss, A., Champollion, N., Fujita, K., … Zekollari, H. (2020). Partitioning the uncertainty of ensemble projections of global glacier mass change. *Earth's Future*, *8*(7), e2019EF001470. Retrieved from https://agupubs.onlinelibrary.wiley.com/doi/abs/10.1029/2019EF001470 (e2019EF001470 10.1029/2019EF001470) doi: https://doi.org/10.1029/2019EF001470

Merrill, R. T. (1988). Environmental influences on hurricane intensification. *Journal of Atmospheric Sciences*, *45*(11), 1678 - 1687. Retrieved from https://journals.ametsoc.org/view/journals/atsc/45/11/1520-0469_1988_045_1678_eiohi_2_0_co_2.xml doi: 10.1175/1520-0469(1988)045⟨1678:EIOHI⟩2.0.CO;2

Oppenheimer, M., Glavovic, B., Hinkel, J., van de Wal, R., Magnan, A. K., Abd-Elgawad, A., ... Sebesvari, Z. (2019). Sea Level Rise and Implications for Low Lying Islands, Coasts and Communities. *IPCC Special Report on the Ocean and Cryosphere in a Changing Climate*, *355*(6321), 126–129.

Peltier, W. R., Argus, D. F., & Drummond, R. (2015). Space geodesy constrains ice age terminal deglaciation: The global ice-6g_c (vm5a) model. *Journal of Geophysical Research: Solid Earth*, *120*(1), 450-487. Retrieved from `https://agupubs.onlinelibrary.wiley.com/doi/abs/10.1002/2014JB011176` doi: https://doi.org/10.1002/2014JB011176

Perrette, M., Landerer, F., Riva, R., Frieler, K., & Meinshausen, M. (2013). A scaling approach to project regional sea level rise and its uncertainties. *Earth System Dynamics*, *4*(1), 11–29. doi: 10.5194/esd-4-11-2013

Rasmussen, D. J., Bittermann, K., Buchanan, M. K., Kulp, S., Strauss, B. H., Kopp, R. E., & Oppenheimer, M. (2018, mar). Extreme sea level implications of 1.5 °c, 2.0 °c, and 2.5 °c temperature stabilization targets in the 21st and 22nd centuries. *Environmental Research Letters*, *13*(3), 034040. Retrieved from `https://doi.org/10.1088/1748-9326/aaac87` doi: 10.1088/1748-9326/aaac87

Reed, A. J., Mann, M. E., Emanuel, K. A., Lin, N., Horton, B. P., Kemp, A. C., & Donnelly, J. P. (2015). Increased threat of tropical cyclones and coastal flooding to new york city during the anthropogenic era. *Proceedings of the National Academy of Sciences*, *112*(41), 12610–12615. Retrieved from `https://www.pnas.org/content/112/41/12610` doi: 10.1073/pnas.1513127112

Resio, D. T., & Irish, J. L. (2015). Tropical Cyclone Storm Surge Risk. , 74–84. doi: 10.1007/s40641-015-0011-9

Rignot, E., Mouginot, J., Morlighem, M., Seroussi, H., & Scheuchl, B. (2014). Widespread, rapid grounding line retreat of pine island, thwaites, smith, and kohler glaciers, west antarctica, from 1992 to 2011. *Geophysical Research Letters*, *41*(10), 3502-3509. Retrieved from `https://agupubs.onlinelibrary.wiley.com/doi/abs/10.1002/2014GL060140` doi: https://doi.org/10.1002/2014GL060140

Rios-Berrios, R., & Torn, R. D. (2017). Climatological analysis of tropical cyclone intensity changes under moderate vertical wind shear. *Monthly Weather Review*, *145*(5), 1717 - 1738. Retrieved from `https://journals.ametsoc.org/view/journals/mwre/145/5/mwr-d-16-0350.1.xml` doi: 10.1175/MWR-D-16-0350.1

Sobel, A. H., Camargo, S. J., Hall, T. M., Lee, C.-Y., Tippett, M. K., & Wing, A. A. (2016). Human influence on tropical cyclone intensity. *Science*, *353*(6296), 242–246. Retrieved from `https://science.sciencemag.org/content/353/6296/242` doi: 10.1126/science.aaf6574

Tamisiea, M. E., & Mitrovica, J. X. (2011). The moving boundaries of sea level change: Understanding the origins of geographic variability. *Oceanography*.

Tang, B., & Camargo, S. J. (2014). Environmental control of tropical cyclones in cmip5: A ventilation perspective. *Journal of Advances in Modeling Earth Systems*, *6*(1), 115-128. Retrieved from `https://agupubs.onlinelibrary.wiley.com/doi/abs/10.1002/2013MS000294` doi: https://doi.org/10.1002/2013MS000294

Tebaldi, C., Strauss, B. H., & Zervas, C. E. (2012, mar). Modelling sea level rise impacts on storm surges along US coasts. *Environmental Research Letters*, *7*(1), 014032. Retrieved from `https://doi.org/10.1088/1748-9326/7/1/014032` doi: 10.1088/1748-9326/7/1/014032

Ting, M., Kossin, J., Camargo, S., & Li, C. (2019, 05). Past and future hurricane intensity change along the u.s. east coast. *Scientific Reports*, *9*. doi: 10.1038/s41598-019-44252-w

Trenberth, K., Fasullo, J., & Shepherd, T. (2015, 07). Attribution of climate extreme events. *Nature Climate Change*, *5*, 725-730. doi: 10.1038/nclimate2657

Vecchi, G. A., Delworth, T. L., Murakami, H., Underwood, S. D., Wittenberg, A. T., Zeng, F., ... Yang, X. (2019). *Tropical cyclone sensitivities to CO2 doubling: roles of atmospheric resolution, synoptic variability and background climate changes* (Vol. 53) (No. 9-10). Springer Berlin Heidelberg. Retrieved from `https://doi.org/10.1007/s00382-019-04913-y` doi: 10.1007/s00382-019-04913-y

Vecchi, G. A., & Soden, B. J. (2007a). Effect of remote sea surface temperature change on tropical cyclone potential intensity. *Nature*, *450*, 1066-1070.

Vecchi, G. A., & Soden, B. J. (2007b). Global warming and the weakening of the tropical circulation. *Journal of Climate*, *20*(17), 4316 - 4340. Retrieved from `https://journals.ametsoc.org/view/journals/clim/20/17/jcli4258.1.xml` doi: 10.1175/JCLI4258.1

Vecchi, G. A., & Soden, B. J. (2007c). Increased tropical Atlantic wind shear in model projections of global warming. *Geophysical Research Letters*, *34*(8), 1–5. doi: 10.1029/2006GL028905

Vega-Westhoff, B., Sriver, R. L., Hartin, C., Wong, T. E., & Keller, K. (2020). The role of climate sensitivity in upper-tail sea level rise projections. *Geophysical Research Letters*, *47*(6), e2019GL085792. Retrieved from `https://agupubs.onlinelibrary.wiley.com/doi/abs/10.1029/2019GL085792` (e2019GL085792 2019GL085792) doi: https://doi.org/10.1029/2019GL085792

Villarini, G., & Vecchi, G. A. (2013). Projected increases in North Atlantic tropical cyclone intensity from CMIP5 models. *Journal of Climate*, *26*(10), 3231–3240. doi: 10.1175/JCLI-D-12-00441.1

Vousdoukas, M., Mentaschi, L., Voukouvalas, E., Verlaan, M., Jevrejeva, S., Jackson, L., & Feyen, L. (2018, 06). Global probabilistic projections of extreme sea levels show intensification of coastal flood hazard. *Nature Communications*, *9*. doi: 10.1038/s41467-018-04692-w

Wahl, T., Jain, S., Bender, J., Meyers, S. D., & Luther, M. E. (2015). Increasing risk of compound flooding from storm surge and rainfall for major US cities. *Nature Climate Change*, *5*(12), 1093–1097. doi: 10.1038/nclimate2736

Wang, Soden, B. J., Yang, W., & Vecchi, G. A. (2021). Compensation between cloud feedback and aerosol-cloud interaction in cmip6 models. *Geophysical Research Letters*, *48*(4), e2020GL091024. Retrieved from `https://agupubs.onlinelibrary.wiley.com/doi/abs/10.1029/2020GL091024` (e2020GL091024 2020GL091024) doi: https://doi.org/10.1029/2020GL091024

Wang, & Toumi, R. (2021). Recent migration of tropical cyclones toward coasts. *Science*, *371*(6528), 514–517. doi: 10.1126/science.abb9038

Westerink, J., Luettich, R., Jr, Blain, C., & Scheffner, N. (1994, 01). Adcirc: An advanced three-dimensional circulation model for shelves, coasts, and estuaries. report 2. user's manual for adcirc-2ddi. , 168.

Woodruff, J. D., Irish, J. L., & Camargo, S. J. (2013). Coastal flooding by tropical cyclones and sea-level rise. *Nature*, *504*(7478), 44–52. doi: 10.1038/nature12855

Yamada, Y., Oouchi, K., Satoh, M., Tomita, H., & Yanase, W. (2010). Projection of changes in tropical cyclone activity and cloud height due to greenhouse warming: Global cloud-system-resolving approach. *Geophysical Research Letters*, *37*(7), 1–5. doi: 10.1029/2010GL042518

Yin, J., Griffies, S. M., Winton, M., Zhao, M., & Zanna, L. (2020). Response of Storm-Related Extreme Sea Level along the U.S. Atlantic Coast to Combined Weather and Climate Forcing. *Journal of Climate*, *33*(9), 3745–3769. Retrieved from `https://doi.org/10.1175/JCLI-D-19-0551.1` doi: 10.1175/JCLI-D-19-0551.1

Zelinka, M. D., Myers, T. A., McCoy, D. T., Po-Chedley, S., Caldwell, P. M., Ceppi, P., ... Taylor, K. E. (2020). Causes of higher climate sensitivity in cmip6 models. *Geophysical Research Letters*, *47*(1), e2019GL085782. Retrieved from `https://agupubs.onlinelibrary.wiley.com/doi/abs/10.1029/2019GL085782` (e2019GL085782 10.1029/2019GL085782) doi: https://doi.org/10.1029/2019GL085782

Zscheischler, J., & Seneviratne, S. I. (2017). Dependence of drivers affects risks associated with compound events. *Science Advances*, *3*(6), 1–11. doi: 10.1126/sciadv.1700263

Zscheischler, J., Westra, S., van den Hurk, B. J. J. M., Seneviratne, S. I., Ward, P. J., Pitman, A., ... Zhang, X. (2018). Future climate risk from compound events. *Nature Climate Change*, *8*(6), 469–477. Retrieved from `https://doi.org/10.1038/s41558-018-0156-3` doi: 10.1038/s41558-018-0156-3

6 Tables

Model	ECS (°C)	GSAT (°C)	Annual frequency	SLR (m)	RMW (%)	PI (%)	TS (%)
GFDL-ESM4	2.6	3.6	0.23	0.68	-11	7.6	-5.9
MIROC6	2.6	4.0	0.53	0.84	-10	8.8	-8.1
MPI-ESM1-2-HR	3.0	3.6	0.26	0.86	-9.3	8.8	-11
MRI-ESM2-0	3.2	4.3	0.13	0.95	-19	22	-13
EC-Earth3	4.3	5.3	2.0	0.97	-22	38	-24
CNRM-CM6-1	4.6	5.6	0.60	1.0	-14	36	-15
IPSL-CM6A-LR	4.6	6.0	1.2	1.0	-18	38	-18
CanESM5	5.6	7.0	0.34	1.1	-15	25	-29

Table 1. Modeled global ECS (°C) and projected changes in relative SLR (m) and TC characteristics at NYC for the CMIP6 subset modeled with ADCIRC. RMW, PI and TS denote the radius of maximum wind speed, maximum wind speed and translation speed, respectively. Estimates of ECS are from Zelinka et al. (2020) and Wang et al. (2021). Change is calculated as the difference between years 1994-2014 of the historical simulation and years 2080-2100 of the high emissions SSP5-8.5.

7 Figures

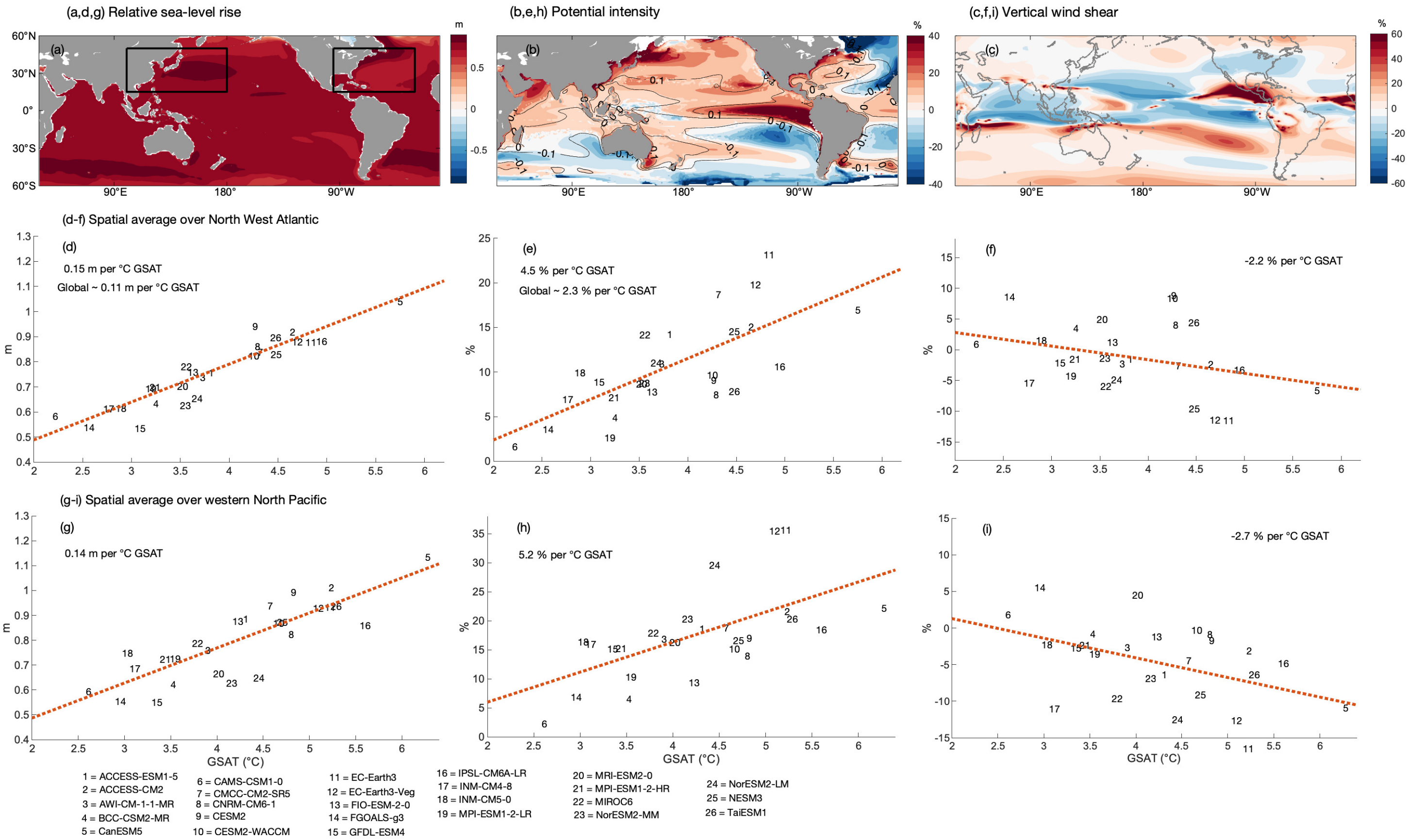

Figure 1. Panels (a–c) show the ensemble mean response of relative sea-level rise (a), potential intensity (b) and vertical wind shear (c). Potential intensity and vertical wind shear are displayed as percentage increases from years 1994-2014 of the historical simulation. Anomalies in potential intensity and vertical wind shear in the Northern Hemisphere are computed over June through November, while anomalies in the Southern Hemisphere are computed over December through May. Contours in (b) show the normalized departure of the local SST change from the tropical-mean (averaged over 35°S - 35°N) SST change. Scatter plots show the spatial averages over the western North Atlantic (d-f) and North West Pacific (e-i): each dot represents a single model. The solid black boxes in (a) show the North West Pacific and western North Atlantic regions.

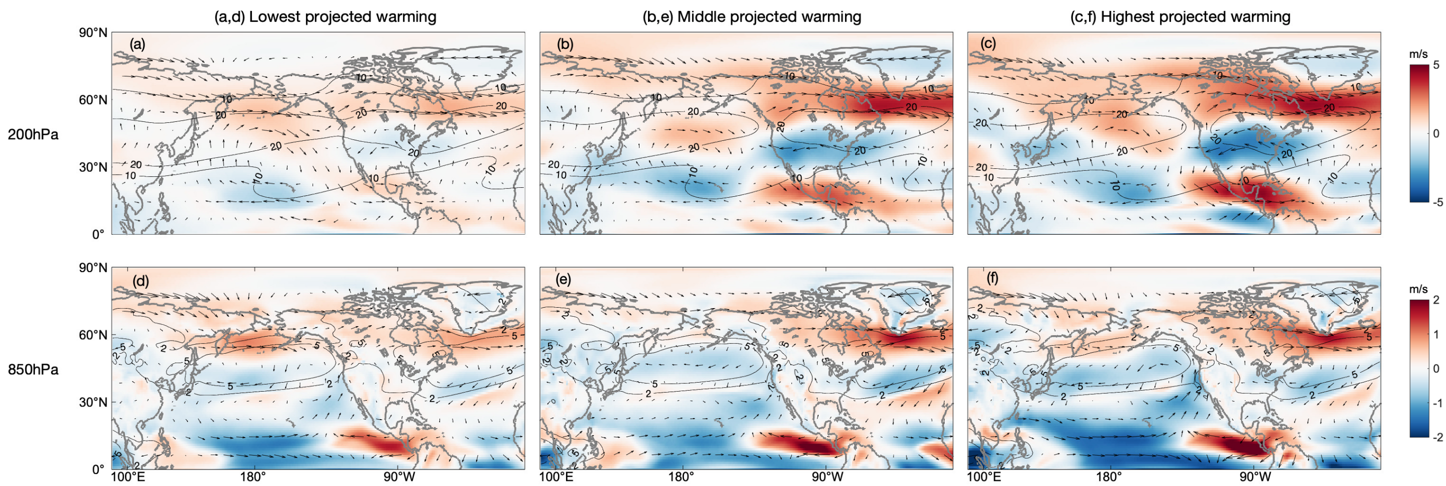

Figure 2. Composites of June-November mean 200hPa (top) and 850 hPa (bottom) horizontal wind vector differences between the average for the SSP5-8.5 (2080-2100) and the historical period (1994-2014). Background colors show speed changes and contours show historical zonal winds. Composites are based on projected GSAT warming. (a,d) Lowest project warming being the average over the models with the lowest third of projected GSAT change; (c,f) highest projected warming models being the average over the top third of project GSAT changes. Anomalies are computed over June through November.

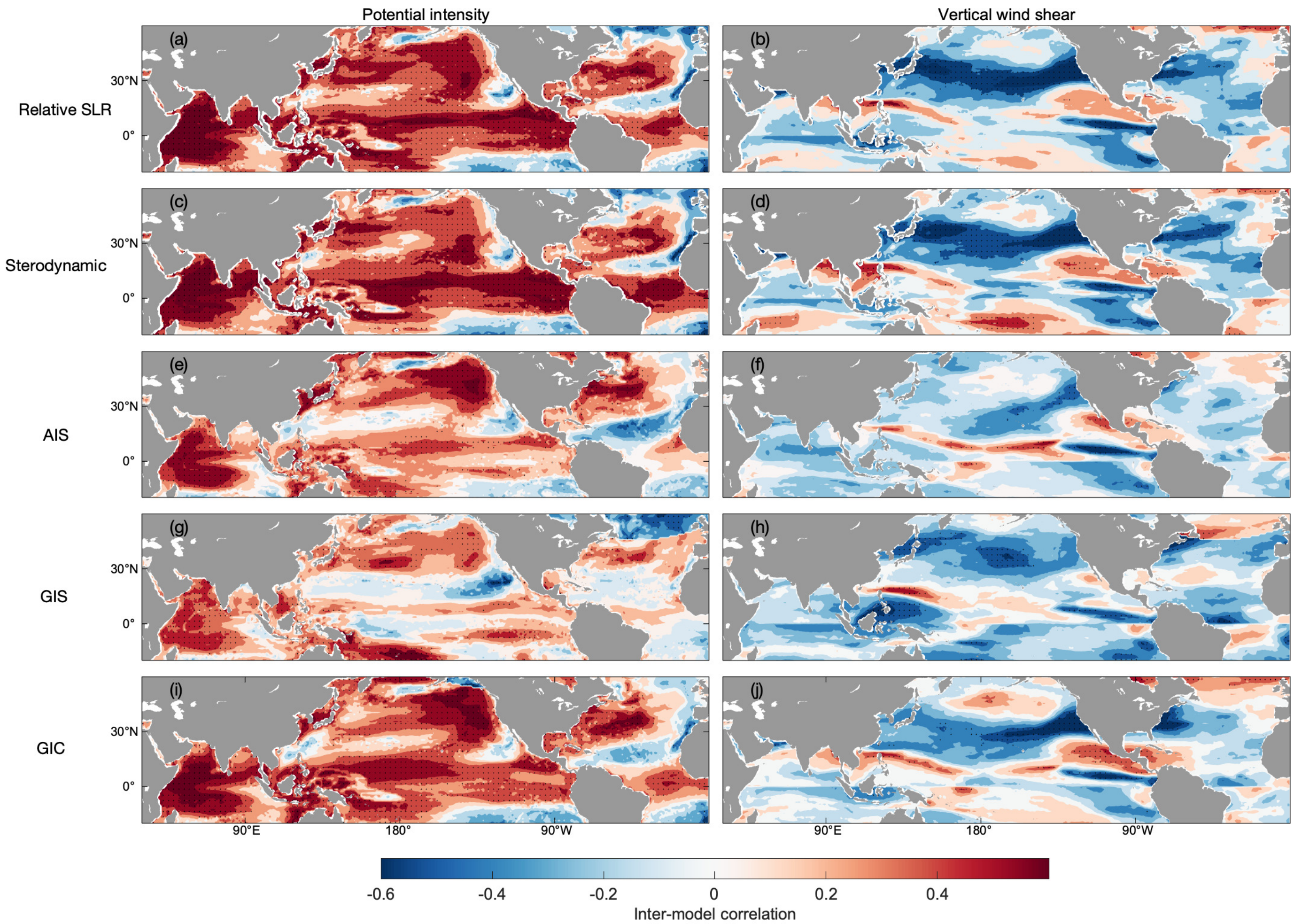

Figure 3. Inter-model correlations between sea-level rise (rows) and potential intensity (left column) and vertical wind shear (right column) for all 26 CMIP6 models. Rows show each component of SLR: relative sea-level rise (a-b), sterodynamic (c-d), Antarctic (e-f), Greenland (g-h) and Glaciers and Ice caps (i-j). Stipples denote correlations significant to 95%.

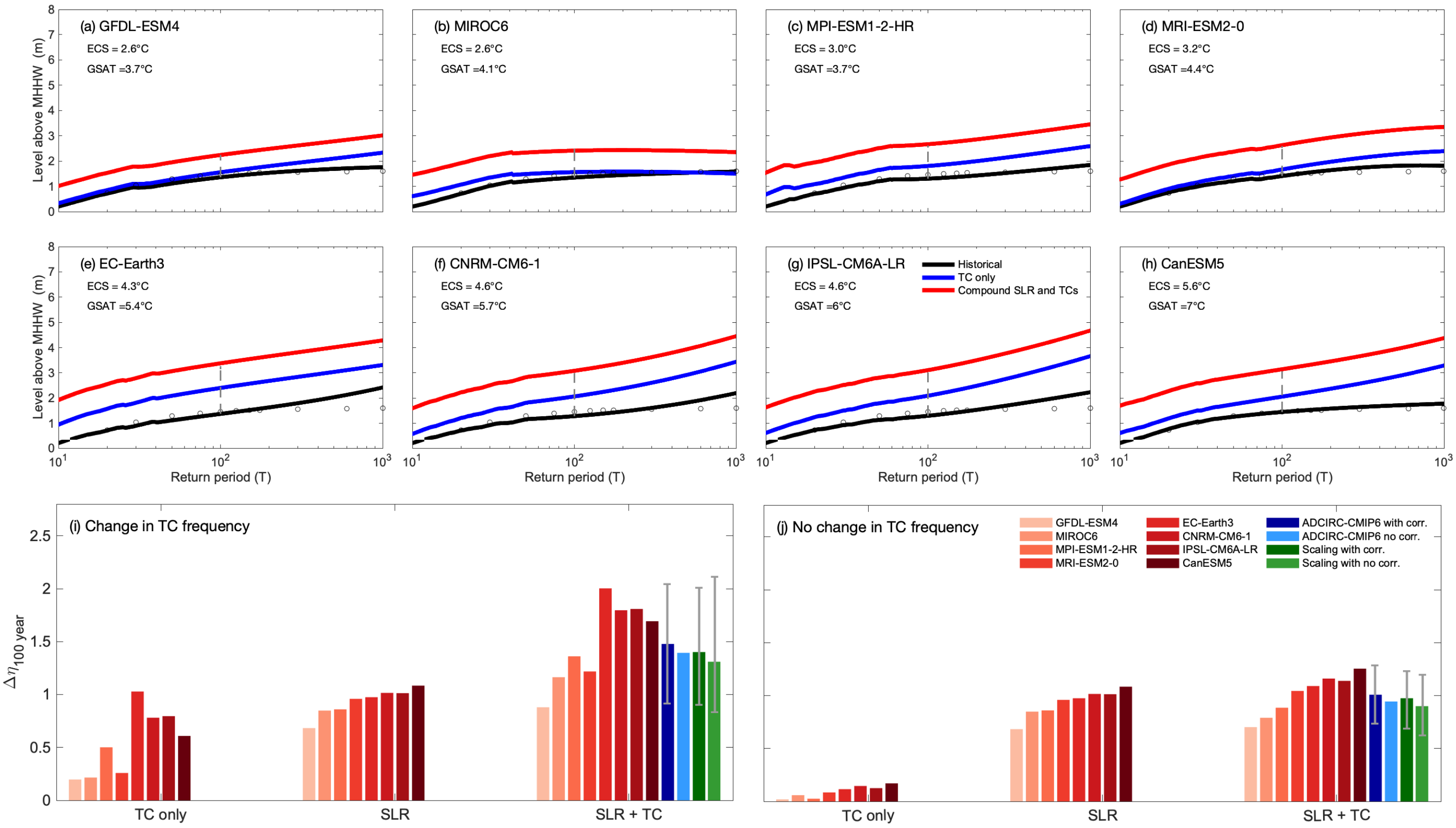

Figure 4. Estimated storm tide return levels for the historical period of 1994-2014 (black) and future period of 2080–2100 (blue: only effects of TC changes, red: compound effects of SLR and TCs) at New York City (a-h). Models are ordered by ascending ECS (Table. 1). Bar charts show the contributions to the change in the 100 year historical storm level, assuming (i) change and (j) no change in TC frequency at NYC. Fig. S10 shows the return period figures assuming no change in frequency of TCs. Storm tide levels are relative to mean higher high water (MHHW, obtained from https://vdatum.noaa.gov). The dark blue bars on (i-j) show the mean of the ADICRC-CMIP6 models that includes correlated changes, whilst the light blue bars show the ADCIRC-CMIP6 projection constructed through convolution (i.e. neglecting correlations). The green bars on (i-j) show the compound changes derived from the scaling method based on the GSAT and SLR projections of all 26 CMIP6 models as described in Section 3.3.3, with the dark green denoting correlated changes and light green neglecting correlated changes. Black dots on (a-h) are empirical estimates. Vertical grey bars (i-j) denote the model ranges.

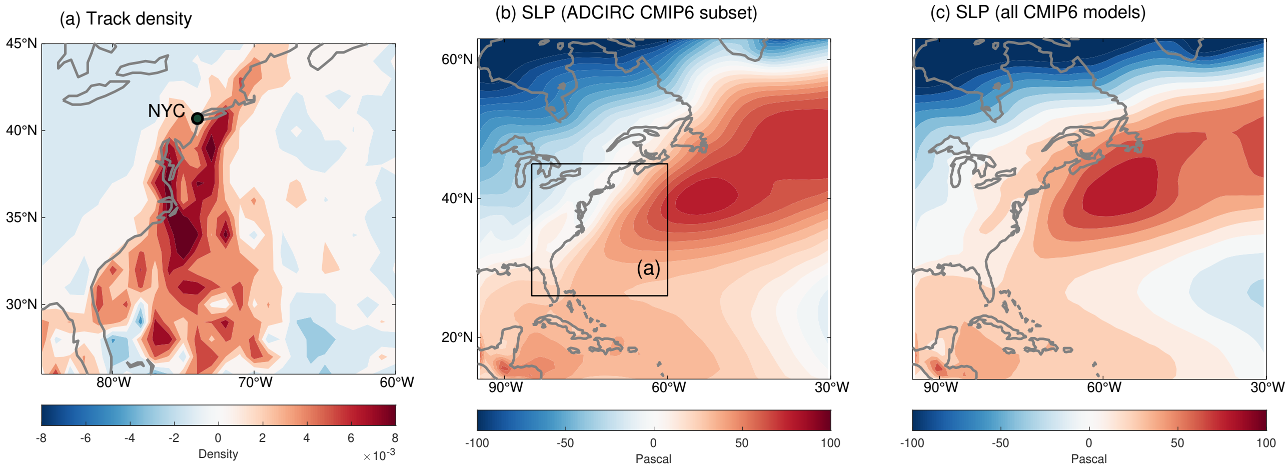

Figure 5. Multimodel mean difference between future and modern synthetic TC track densities assuming no change in TC frequency at NYC (a). Track densities are determined by the sum total of tracks crossing through each grid box over 20-year periods from 2080–2100 and 1994–2014, divided by the area of that grid box and the number of years. (b-c) Mean sea-level pressure (SLP) differences (pascals) averaged over June - November for the eight CMIP6 modeled with ADCIRC (b) and for all 26 CMIP6 used in this study (c).

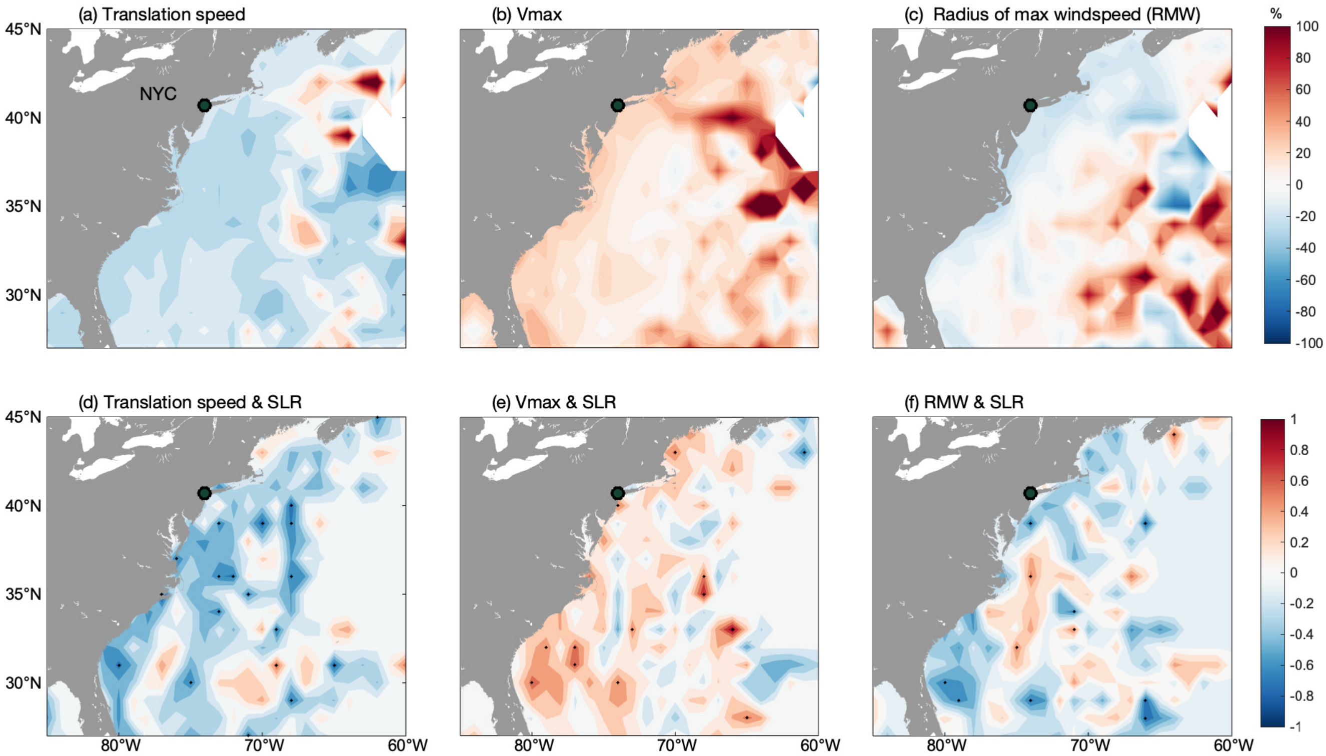

Figure 6. (a-c) Multimodel mean projected changes in TC intensity, radius of maximum wind and speed translation speed shown as percentage increases from years 1994-2014 of the historical simulation. (d-f) Inter-model correlations between projected changes in TC characteristics and relative SLR.

Supporting Information for "Correlation between sea-level rise and aspects of future tropical cyclone activity in CMIP6 models"

Joseph W. Lockwood[1], Michael Oppenheimer[1,2,3], Ning Lin[4], Robert E. Kopp[5,6], Gabriel A. Vecchi[1,3,7] and Avantika Gori[4]

[1]Department of Geoscience, Princeton University, NJ 08544, USA

[2]Princeton School of Public and International Affairs, Princeton University, Princeton, NJ 08544, USA

[3]High Meadows Environmental Institute, Princeton, NJ, USA

[4]Civil and Environmental Engineering, Princeton University, Princeton, NJ 08544, USA

[5]Institute of Earth, Ocean, and Atmospheric Sciences, Rutgers University, 71 Dudley Road, Suite 205, New Brunswick, NJ 08901, USA

[6]Department of Earth and Planetary Sciences, Rutgers University, Piscataway, NJ, USA

[7]Atmospheric and Oceanic Sciences Program, Princeton University, Princeton, NJ, USA

Contents of this file

1. Text S1

1.1. Sterodynamic sea-level

Most CMIP6 models utilized in this study are based on the Boussinesq approximation, conserving volume, not mass. As shown by Greatbatch (1994), such models are unable to capture the global mean thermosteric SLR associated with changes in the global mean density, with the bottom pressure also corrupted due to spurious mass sources required to conserve volume rather than mass. As some models used in this study do not have zostoga output, we calculate h_θ using potential temperature (thetao) referenced to the first year of each simulation (Griffies et al., 2016):

$$h_\theta = \left(\frac{V^0}{A}\right)\left(1 - \frac{\rho(\theta^\eta, S^0, p^0)}{\rho^0}\right) \tag{1}$$

where V^0 is the reference global volume of seawater and A is the area of the global ocean surface. The ocean density (ρ) in the numerator is computed as a function of the time evolving potential temperature, with salinity and pressure held constant at their reference value. Although halosteric sea-level change due to salinity changes, can be locally of the same order of magnitude as thermosteric, global-mean halosteric sea-level change is practically zero, and thus is often neglected. Spurious long-term drift is removed using at least 250 years of the models pre-industrial control simulation (piControl) (Gupta et al., 2013).

1.2. AIS SMB

Future Antarctic SMB is expected to increase in response to atmospheric warming as a result of enhanced snowfall, while runoff remains small (Palerme et al., 2017; Gorte et al., 2020). We construct anomalies in Antarctic SMB and its driving components, from the finding in the high resolution regional atmospheric model MAR (Modele Atmospherique Regional) forced by an ensemble of CMIP6 models, that SMB changes are strongly correlated with the near-surface warming of the forcing ESMs around the AIS (Kittel et al., 2021):

$$\Delta SMB_{AIS} = TAS_{90-60^{\circ}S} + 115.4TAS_{90-60^{\circ}S} - 11.1 \tag{2}$$

where $TAS_{90-60^{\circ}S}$ is the surface temperature anomaly averaged between $90 - 60^{\circ}S$.

Additionally, we estimate sea-level contribution from changes in Antarctic SMB from a parameterization based on regional climate output of different ESMs (Gregory & Huybrechts, 2006). This parameterization from Gregory and Huybrechts (2006) is based on the finding that net accumulation over the Antarctic ice-sheet increases with regional atmospheric warming:

$$\Delta SMB_{AIS} = AP\Delta T \tag{3}$$

Here, A is the time-mean snowfall accumulation during 1986-2010, equal to 1983 ± 122 Gt yr^{-1} (Lenaerts et al., 2012). Factor P is the rate of increased accumulation per degree of regional atmospheric warming relative to this reference period, equal to 5.15% per degree, and ΔT is the anomaly in atmospheric temperature averaged over the Antarctic ice-sheet. Frieler et al. (2015) suggested an increase in accumulation linked to air temperature of 5-6% per degree Celsius, which is confirmed by SMB reconstructions from ice cores over the 20th century (Medley & Thomas, 2019). These two methods show good agreement (Fig. S17).

References

Frieler, K., Clark, P. U., He, F., Buizert, C., Reese, R., Ligtenberg, S. R. M., ... Levermann, A. (2015). Consistent evidence of increasing Antarctic accumulation with warming. , *5*(April), 1–5. doi: 10.1038/NCLIMATE2574

Fürst, J. J., Goelzer, H., & Huybrechts, P. (2015). Ice-dynamic projections of the greenland ice sheet in response to atmospheric and oceanic warming. *The Cryosphere*, *9*(3), 1039–1062. Retrieved from https://tc.copernicus.org/articles/9/1039/2015/ doi: 10.5194/tc-9-1039-2015

Gorte, T., Lenaerts, J. T. M., & Medley, B. (2020). Scoring antarctic surface mass balance in climate models to refine future projections. *The Cryosphere*, *14*(12), 4719–4733. Retrieved from https://tc.copernicus.org/articles/14/4719/2020/ doi: 10.5194/tc-14-4719-2020

Greatbatch, R. J. (1994). A note on the representation of steric sea level in models that conserve volume rather than mass. *Journal of Geophysical Research: Oceans*, *99*(C6), 12767-12771. Retrieved from https://agupubs.onlinelibrary.wiley.com/doi/abs/10.1029/94JC00847 doi: https://doi.org/10.1029/94JC00847

Gregory, J., & Huybrechts, P. (2006). Ice-sheet contributions to future sea-level change. *Philosophical Transactions of the Royal Society A: Mathematical, Physical and Engineering Sciences*, *364*(1844), 1709-1732. doi: 10.1098/rsta.2006.1796

Griffies, S. M., Danabasoglu, G., Durack, P. J., Adcroft, A. J., Balaji, V., Böning, C. W., ... Yeager, S. G. (2016). OMIP contribution to CMIP6: Experimental and diagnostic protocol for the physical component of the Ocean Model Intercomparison Project. *Geoscientific Model Development*, *9*(9), 3231–3296. doi: 10.5194/gmd-9-3231-2016

Gupta, A. S., Jourdain, N. C., Brown, J. N., & Monselesan, D. (2013). Climate drift in the CMIP5 models. *Journal of Climate*, *26*(21), 8597–8615. doi: 10.1175/JCLI-D-12-00521.1

Kittel, C., Amory, C., Agosta, C., Jourdain, N. C., Hofer, S., Delhasse, A., ... Fettweis, X. (2021). Diverging future surface mass balance between the Antarctic ice shelves and grounded ice sheet. , 1215–1236.

Lenaerts, J. T., Van Den Broeke, M. R., Van De Berg, W. J., Van Meijgaard, E., & Kuipers Munneke, P. (2012). A new, high-resolution surface mass balance map of Antarctica (1979-2010) based on regional atmospheric climate modeling. *Geophysical Research Letters*, *39*(4), 1–5. doi: 10.1029/2011GL050713

Medley, B., & Thomas, E. R. (2019). Increased snowfall over the Antarctic Ice Sheet mitigated twentieth-century sea-level rise. *Nature Climate Change*, *9*(January). Retrieved from `http://dx.doi.org/10.1038/s41558-018-0356-x` doi: 10.1038/s41558-018-0356-x

Palerme, C., Genthon, C., Claud, C., Kay, J., Wood, N., & L'Ecuyer, T. (2017, 01). Evaluation of current and projected antarctic precipitation in cmip5 models. *Climate Dynamics*, *48*. doi: 10.1007/s00382-016-3071-1

Wang, C., Soden, B. J., Yang, W., & Vecchi, G. A. (2021). Compensation between cloud feedback and aerosol-cloud interaction in cmip6 models. *Geophysical Research Letters*, *48*(4), e2020GL091024. Retrieved from `https://agupubs.onlinelibrary.wiley.com/doi/abs/10.1029/2020GL091024` (e2020GL091024 2020GL091024) doi: https://doi.org/10.1029/2020GL091024

Zelinka, M. D., Myers, T. A., McCoy, D. T., Po-Chedley, S., Caldwell, P. M., Ceppi, P.,

. . . Taylor, K. E. (2020). Causes of higher climate sensitivity in cmip6 models. *Geophysical Research Letters*, *47*(1), e2019GL085782. Retrieved from https://agupubs.onlinelibrary.wiley.com/doi/abs/10.1029/2019GL085782 (e2019GL085782 10.1029/2019GL085782) doi: https://doi.org/10.1029/2019GL085782

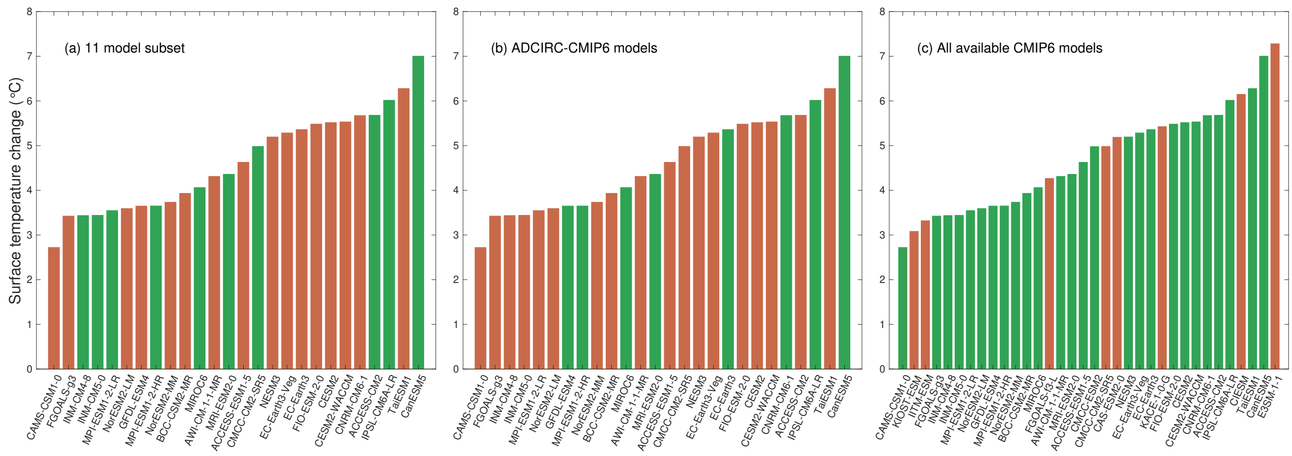

Figure S1. Projections of global mean temperature change (tas) change for (a) the 11 model subset, (b) for the models used in ADCIRC modeling and (c) all 34 CMIP6 models with available tas variable for the simulations and run used in this study. Green denotes models used in analysis.

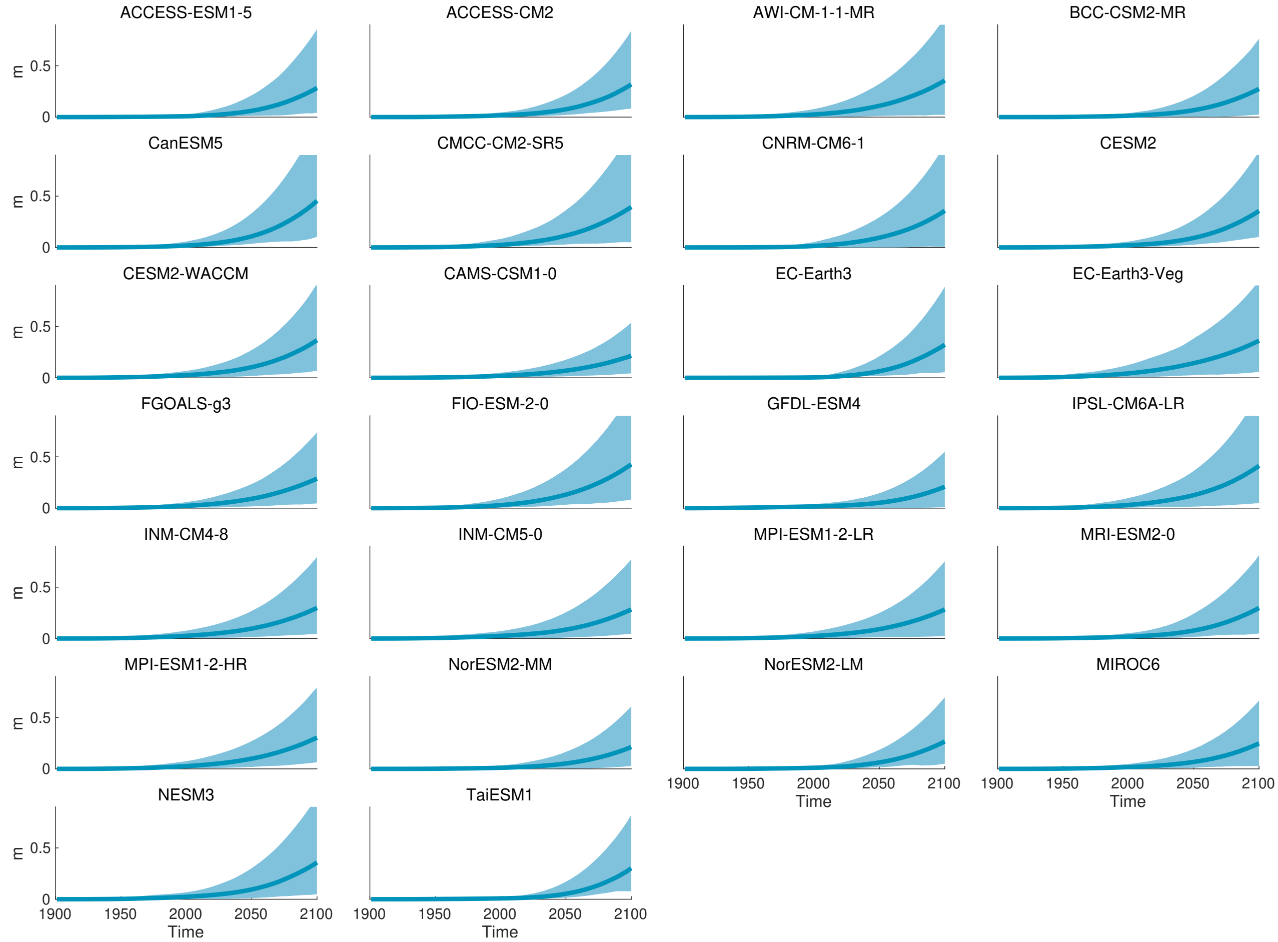

Figure S2. Projection of AIS dynamical SLR for each model, with shading denoting the likely range (66th percentile around the mean).

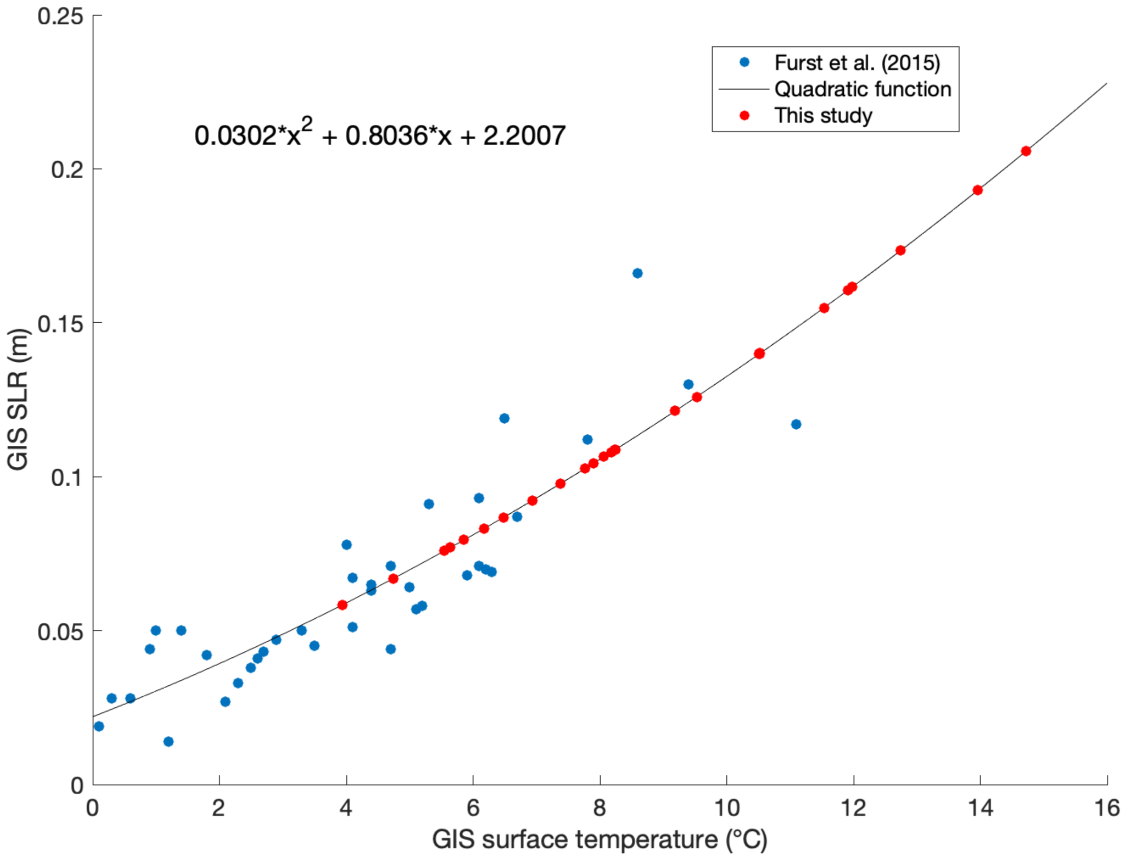

Figure S3. Relationship between Greenland Ice Sheet mass loss and temperature change derived from CMIP5 models in Fürst et al. (2015) (blue points). Red points show the estimates using the CMIP6 models in this study.

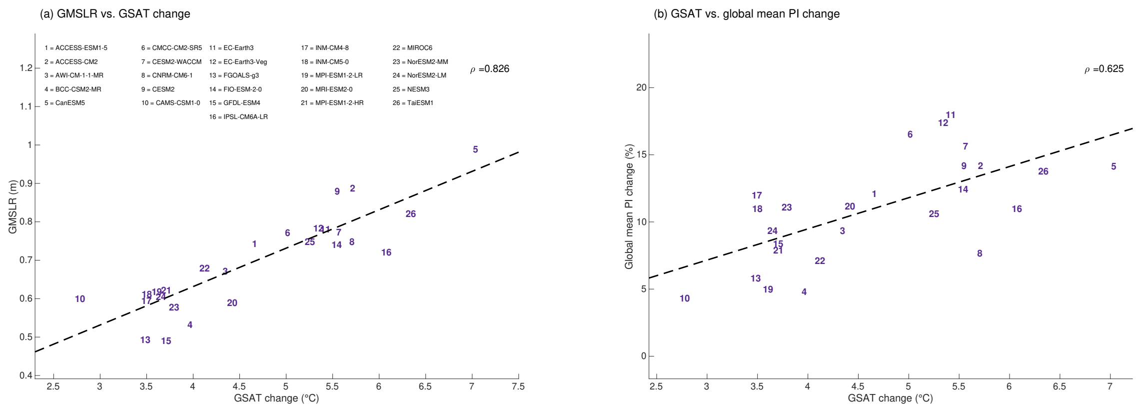

Figure S4. Scatter plots showing (a) global mean sea level rise and global mean temperature change and (b) global potential intensity change and global mean temperature change for each model.

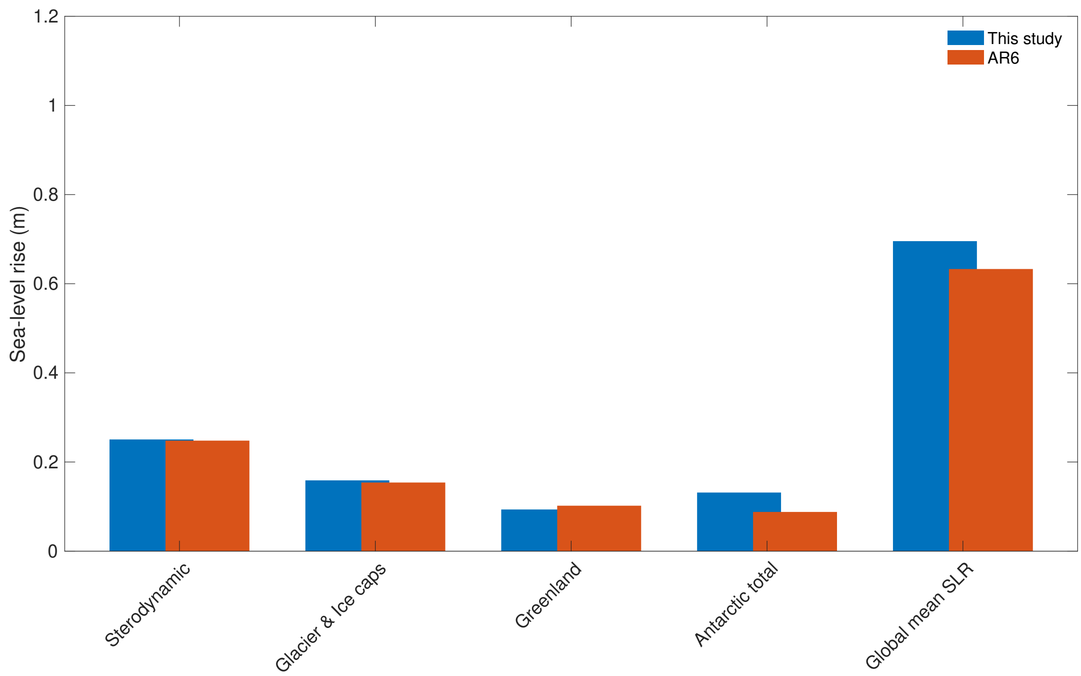

Figure S5. Global mean sea level rise projection comparison between AR6 and this study.

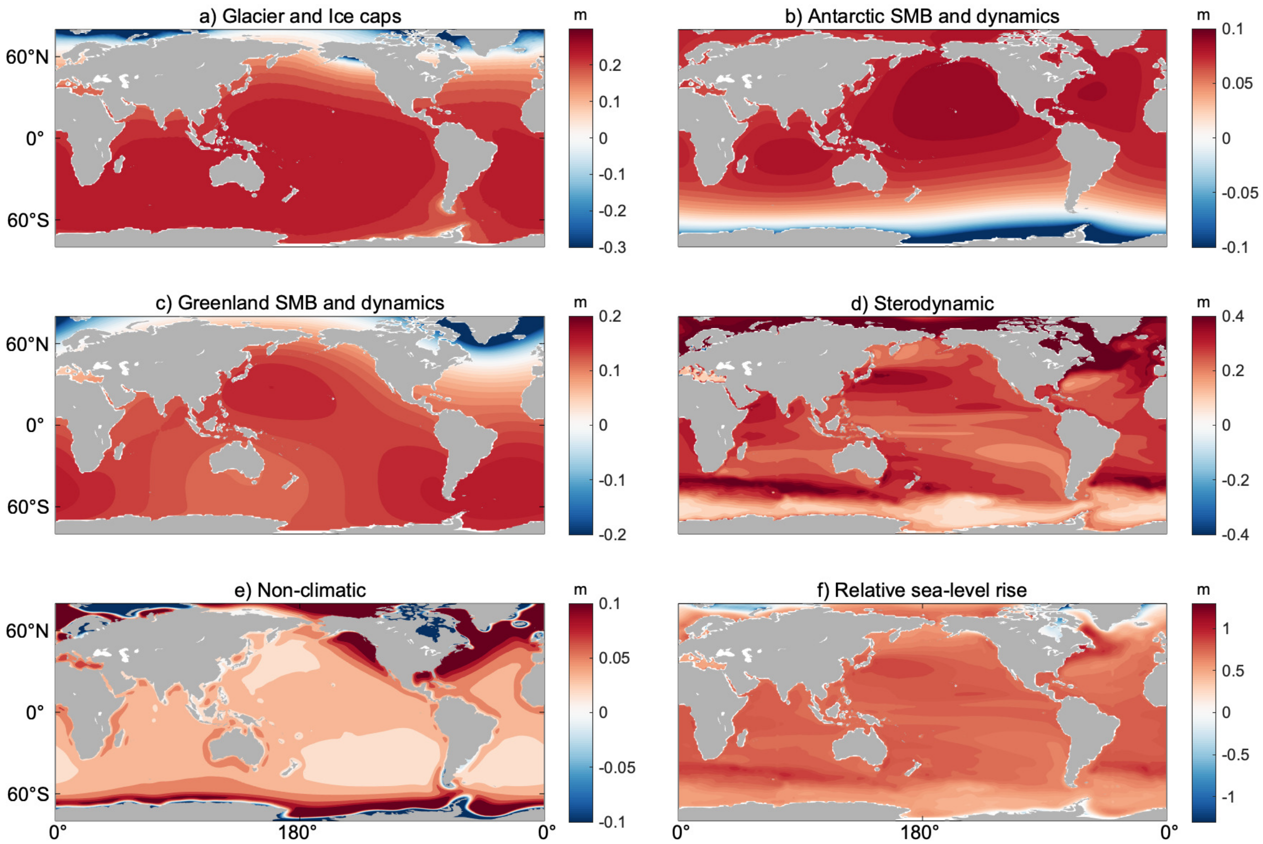

Figure S6. CMIP6 ensemble mean sea-level rise difference maps of (a) GIC, (b) AIS, (c) GIC, (d) sterodynamic, (e) non-climatic and (f) relative SLR for SSP5-8.5.

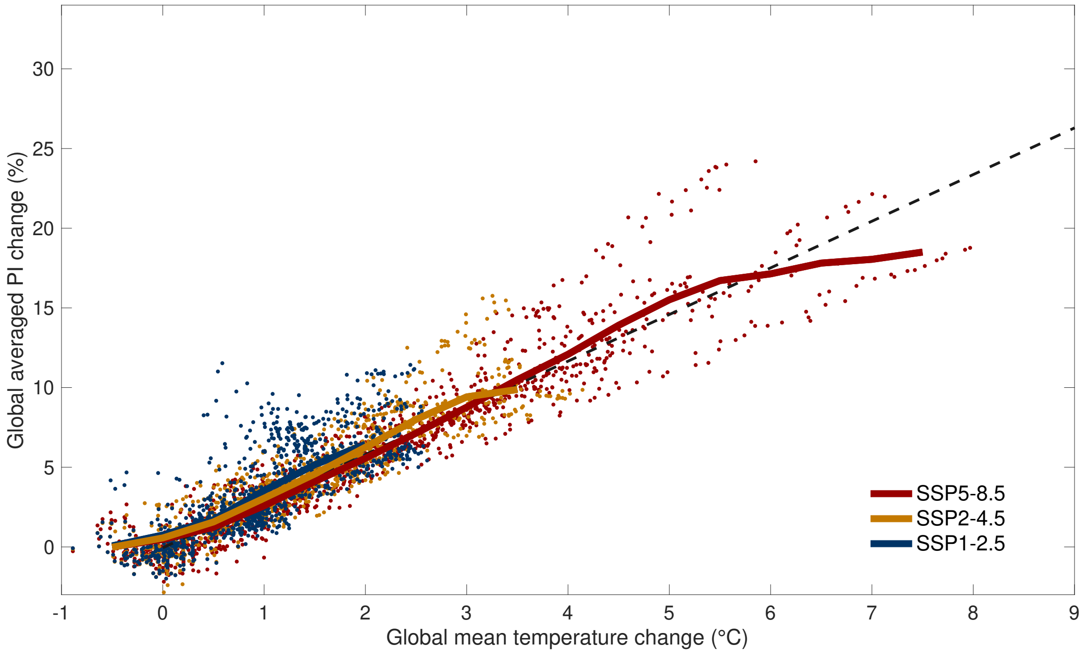

Figure S7. Globally averaged PI change (%) and global mean temperature change for the SSP5-8.5 (red), SSP2-4.5 (yellow) and SSP1-2.5 (blue) scenarios. Each point denotes one year for one model between years 2014 - 2100. Only eleven CMIP6 models are displayed (ACCESS-ESM1-5, ACCESS-CM2, CanESM5, CMCC-CM2-SR5, IPSL-CM6A-LR, INM-CM4-8, INM-CM5-0, MPI-ESM1-2-LR, MRI-ESM2-0, MPI-ESM1-2-HR, MIROC6). These models cover the full range of modeled ECS and GSAT temperature change (Fig. S1).

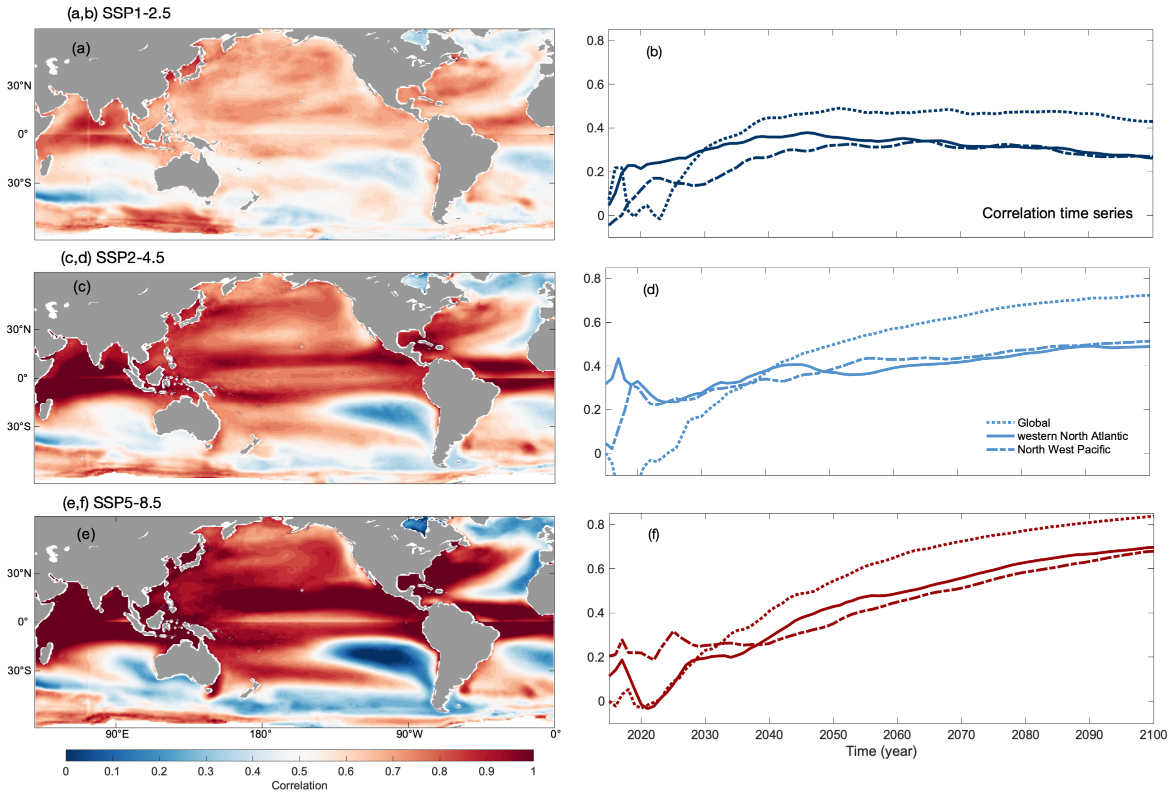

Figure S8. Ensemble averages of intra-model correlations between relative SLR and PI change over space (a,c,e) and time (b,d,f). For each model, correlations are calculated over the 86 years of the SSP1-2.5 (a,b), SSP2-4.5 (c,d) and SSP5-8.5 (e,f) scenarios. Averages are over eleven CMIP6 models (ACCESS-ESM1-5, ACCESS-CM2, CanESM5, CMCC-CM2-SR5, IPSL-CM6A-LR, INM-CM4-8, INM-CM5-0, MPI-ESM1-2-LR, MRI-ESM2-0, MPI-ESM1-2-HR, MIROC6). These models span the full range of modeled GSAT change (Fig. S1). Time-series of correlations (b,d,f) are calculated relative to year 2014.

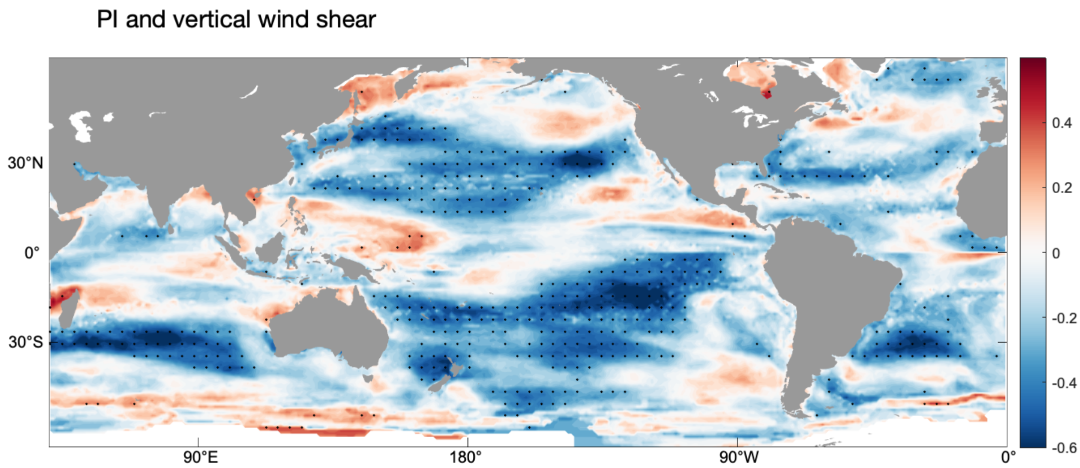

Figure S9. Inter-model correlation between PI and vertical wind shear. Stipples denote correlations significant to 95%.

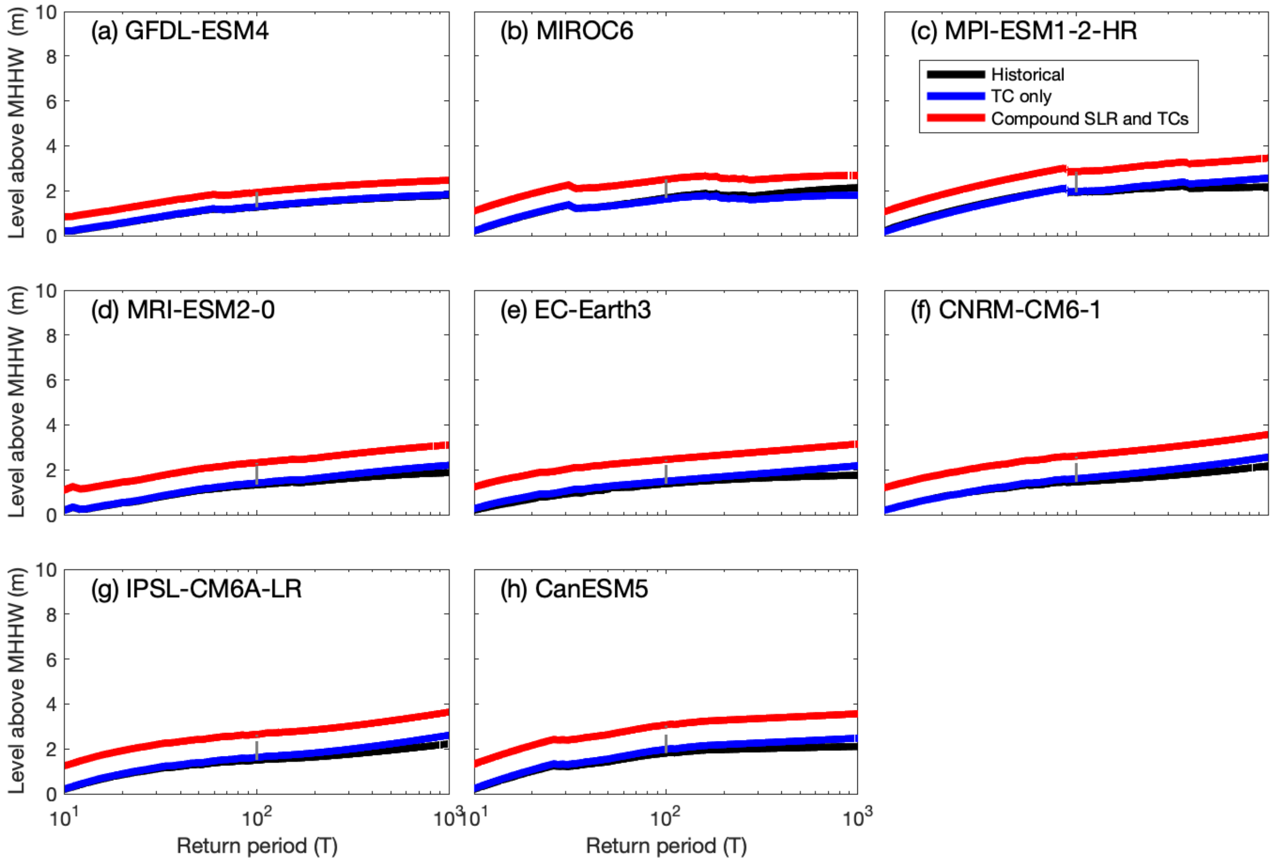

Figure S10. Same as Figure 4, but assuming no change in TC frequency at NYC. Estimated storm tide return levels for the historical period of 1994-2014 (black) and future period of 2080–2100 (blue: only effects of TC changes, red: compound effects of SLR and TCs) at New York City.

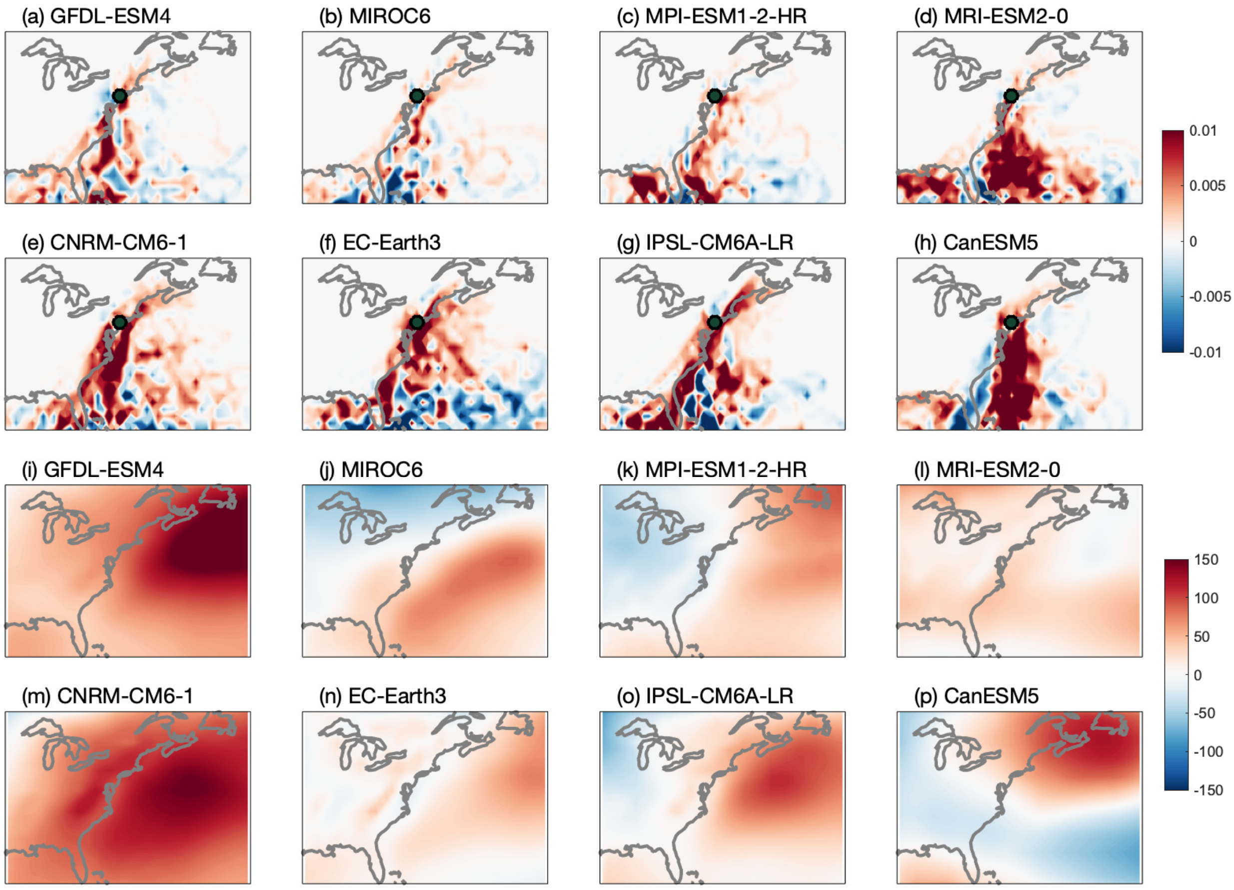

Figure S11. Mean difference between future and modern synthetic TC track densities for each model (a-h). Track densities are determined by the sum total of tracks crossing through each grid box over 20-year periods from 2080–2100 and 1994–2014, divided by the area of that grid box and the number of years. Also shown are the mean sea-level pressure differences (pascals) averaged over June - November for the eight CMIP6 modeled with ADCIRC (i-p).

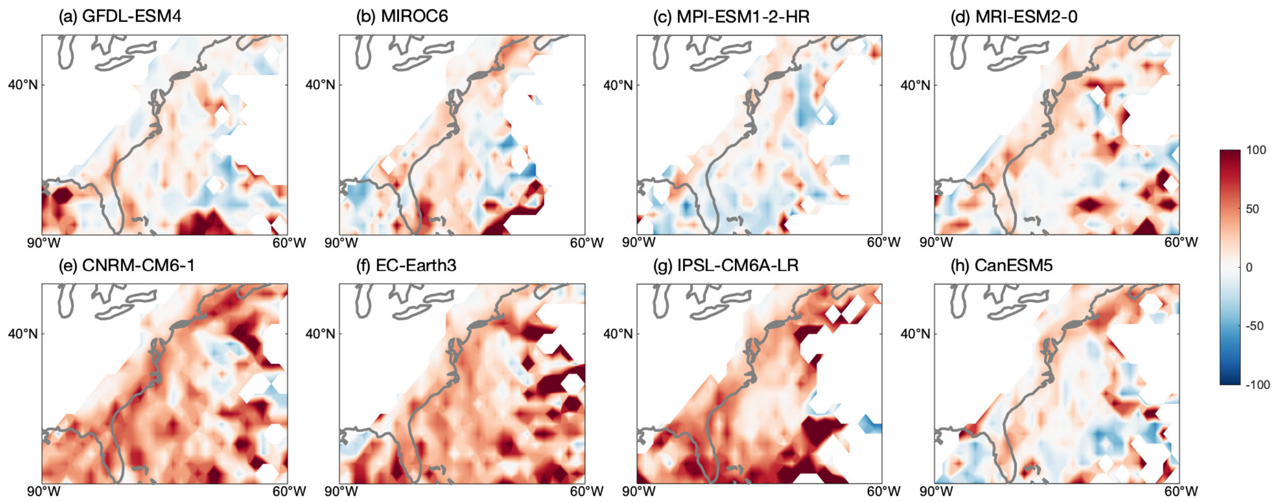

Figure S12. Mean projected changes in Vmax shown as percentage increases from years 1994-2014 of the historical simulation.

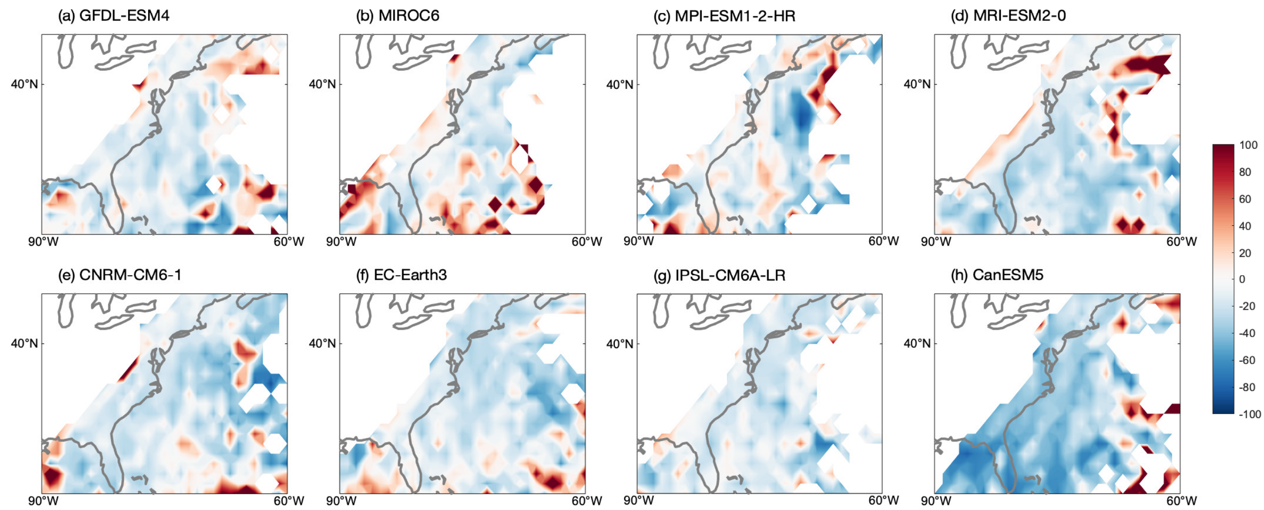

Figure S13. Mean projected changes in translation speed shown as percentage increases from years 1994-2014 of the historical simulation.

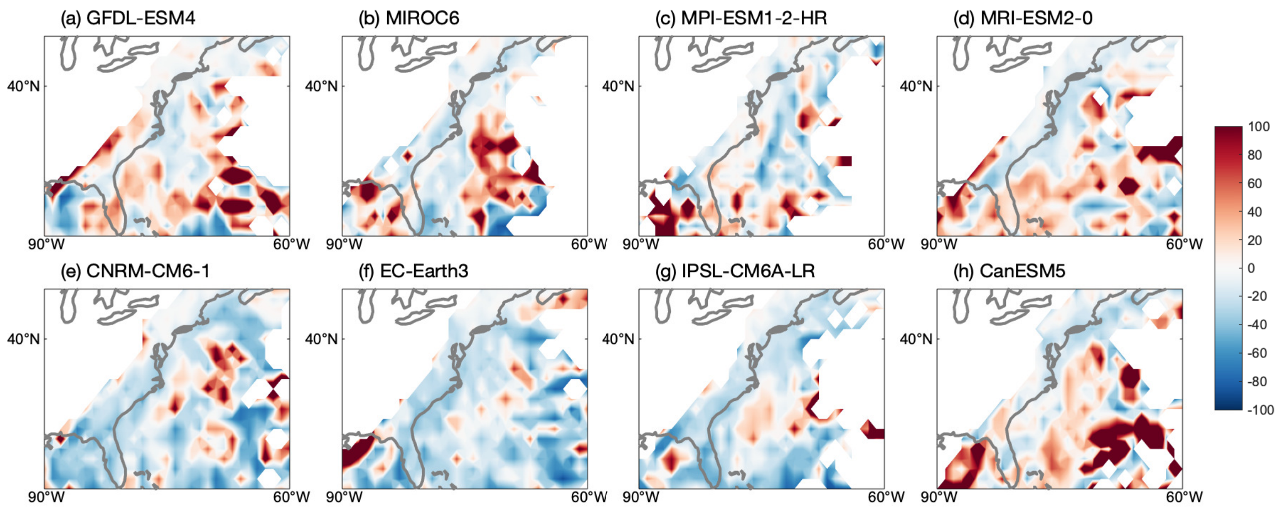

Figure S14. Mean projected changes in radius of maximum wind speed shown as percentage increases from years 1994-2014 of the historical simulation.

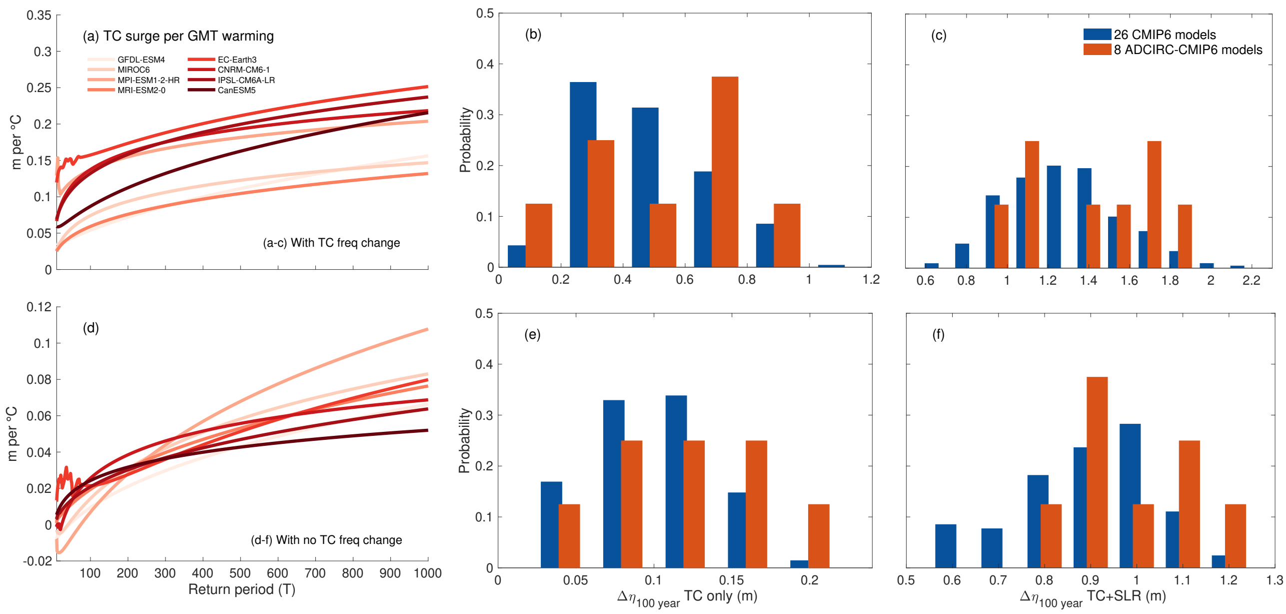

Figure S15. (a,d) Scaling relationships between TC surge changes at NYC and global mean temperature (GSAT) change for the eight ADCIRC-CMIP6 models, assuming change (top) and no change (bottom) in TC frequency. Probability density functions (PDF) show the change to the historical 100 year flood event ($\Delta\eta_{100}$) resulting from TC climatology change (b,e) and both SLR and TC climatology change (c,f) for the ADCIRC-CMIP6 models (red) and all 26 CMIP6 models (blue). To produce the PDFs for all 26 CMIP6 models (blue), we randomly sample one of the eight scaling factors and one of the 26 CMIP6 models GSAT and SLR projections 100,000 times.

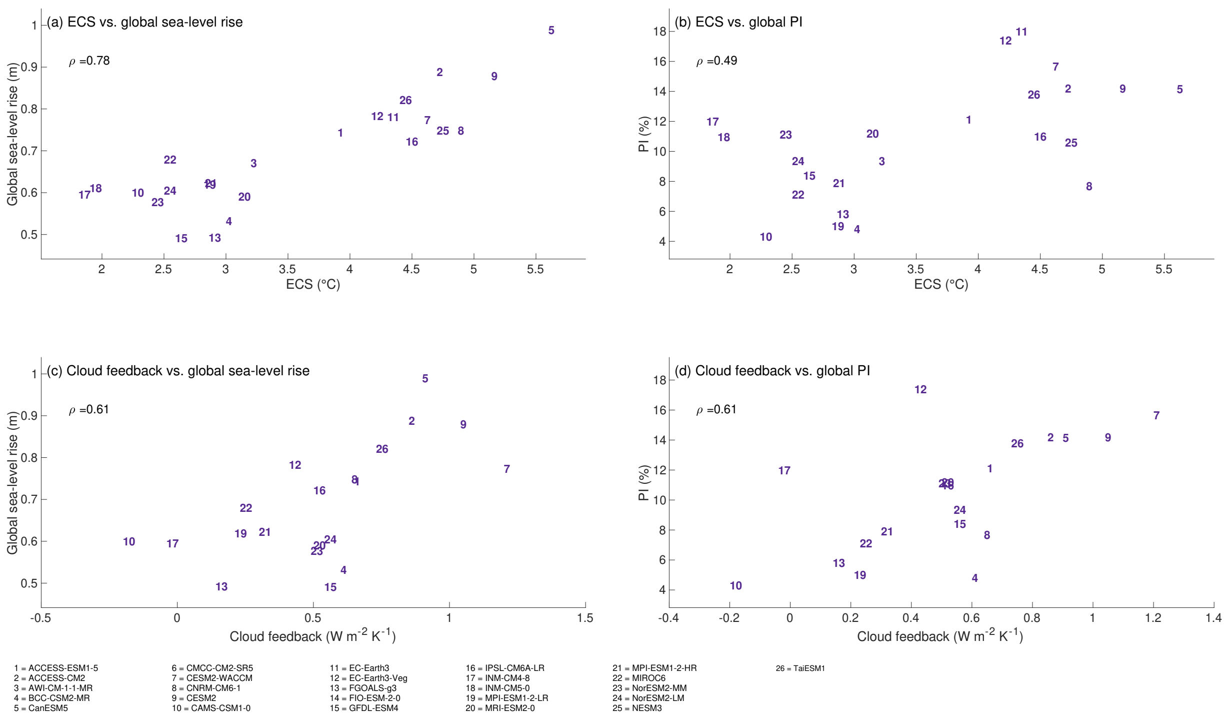

Figure S16. Scatter plots showing global mean sea level rise against effective climate sensitivity (ECS) (a) and cloud feedback (c). Also shown is global averaged potential intensity against ECS (b) and cloud feedback (d). Cloud feedback values are from Wang et al. (2021). ECS values are from Wang et al. (2021) and Zelinka et al. (2020).

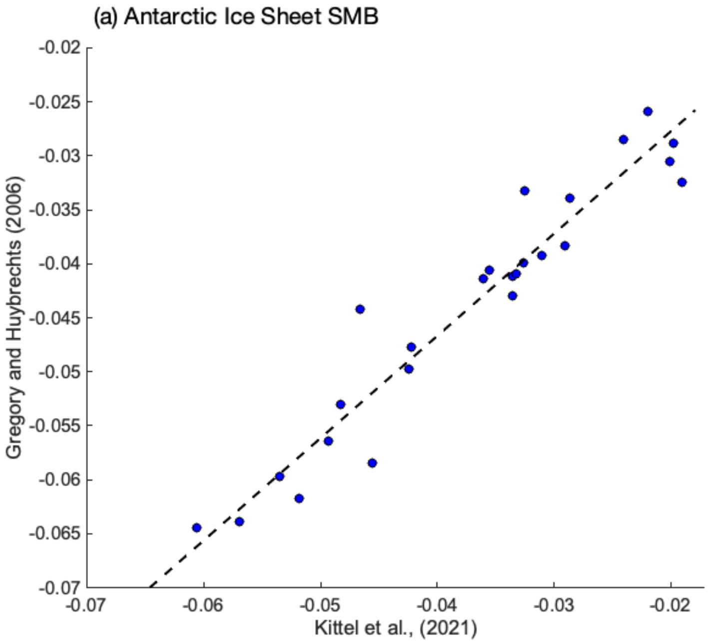

Figure S17. Comparison between the two methods (Gregory and Huybrechts (2006) and Kittel et al. (2021)) used to model Antarctic Ice Sheet surface mass balance changes. Each point denotes one CMIP6 model.